

**Regime shifts in the Changjiang (Yangtze River) Estuary  
The role of concentrated benthic suspensions**

Lin, Jianliang; van Prooijen, Bram C.; Guo, Leicheng; Zhu, Chunyan; He, Qing; Wang, Zheng Bing

**DOI**

[10.1016/j.margeo.2020.106403](https://doi.org/10.1016/j.margeo.2020.106403)

**Publication date**

2021

**Document Version**

Final published version

**Published in**

Marine Geology

**Citation (APA)**

Lin, J., van Prooijen, B. C., Guo, L., Zhu, C., He, Q., & Wang, Z. B. (2021). Regime shifts in the Changjiang (Yangtze River) Estuary: The role of concentrated benthic suspensions. *Marine Geology*, 433, Article 106403. <https://doi.org/10.1016/j.margeo.2020.106403>

**Important note**

To cite this publication, please use the final published version (if applicable).  
Please check the document version above.

**Copyright**

Other than for strictly personal use, it is not permitted to download, forward or distribute the text or part of it, without the consent of the author(s) and/or copyright holder(s), unless the work is under an open content license such as Creative Commons.

**Takedown policy**

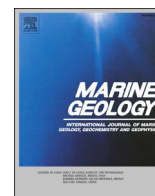
Please contact us and provide details if you believe this document breaches copyrights.  
We will remove access to the work immediately and investigate your claim.

***Green Open Access added to TU Delft Institutional Repository***

***'You share, we take care!' - Taverne project***

**<https://www.openaccess.nl/en/you-share-we-take-care>**

Otherwise as indicated in the copyright section: the publisher is the copyright holder of this work and the author uses the Dutch legislation to make this work public.



## Regime shifts in the Changjiang (Yangtze River) Estuary: The role of concentrated benthic suspensions

Jianliang Lin<sup>a,b</sup>, Bram C. van Prooijen<sup>b</sup>, Leicheng Guo<sup>a</sup>, Chunyan Zhu<sup>a,b</sup>, Qing He<sup>a,\*</sup>, Zheng Bing Wang<sup>a,b,c</sup>

<sup>a</sup> State Key Laboratory of Estuarine and Coastal Research, East China Normal University, Shanghai 200241, China

<sup>b</sup> Faculty of Civil Engineering and Geosciences, Delft University of Technology, Delft, the Netherlands

<sup>c</sup> Deltares, Delft, the Netherlands

### ARTICLE INFO

#### Keywords:

Concentrated benthic suspensions  
Sediment trapping  
Turbulence damping  
Drag reduction  
Estuarine turbidity maximum  
Channel deepening

### ABSTRACT

Channel deepening often triggers positive feedback between tidal deformation, sediment import and drag reduction, which leads to the regime shift in estuaries from low-turbid to hyper-turbid state. In this study, a transition in profiles of suspended sediment concentration (SSC) is hypothesised by including a positive feedback loop of vertical mixing and settling. Such a hypothesis is validated by the historical observations in the North Passage of Changjiang (Yangtze River) Estuary, with decreasing SSC in mid-lower layers and increasing SSC near the bed after the deepening. A mobile pool of concentrated benthic suspensions (CBS) develops in the North Passage, with a tidally averaged length of ~20 km and a mean thickness of ~4 m. The width of the CBS pool is limited (<1 km) as the CBS is concentrated in the Deepwater Navigational Channel. The movements of the CBS pool, combined with tidal asymmetry (e.g., slack-water asymmetry and lateral flow asymmetry), results in sediment trapping in the middle reaches and on the south flank of the channel. Observations by a bottom tripod system show the response of friction/drag coefficient to sediment concentration: (1) nearly linear decrease within low SSC (<10 kg/m<sup>3</sup>); (2) constant and minimum coefficient (with drag reduction up to 60–80%) in the presence of CBS (10–80 kg/m<sup>3</sup>). An empirical relationship was derived, which can be used to predict the friction coefficient and the magnitude of drag reduction for sediment transport studies, particularly for modelling regime shifts in estuaries.

### 1. Introduction

In estuaries, one can often observe regions where suspended sediment concentrations (SSC) are higher than in adjacent waters, called estuarine turbidity maxima (ETM). ETMs are of great importance in the natural and socio-economic value of estuaries, by affecting light availability (Yoshiyama and Sharp, 2006; Cloern et al., 2014), oxygen level (Uncles et al., 1998; Talke et al., 2009) and dredging for navigational channels (Liu et al., 2011).

In order to control flooding and accommodate larger ships, many estuaries are heavily engineered, such as deepening by dredging and narrowing by land reclamations. After the engineering, Winterwerp et al. (2013) observed a regime shift in SSC from low- to hyper-turbid state in the Ems Estuary (Netherlands, Germany) and Loire Estuary (France). They attributed this transition to human-made deepening and hypothesised a positive feedback loop for the regime shift in estuaries

(Winterwerp and Wang, 2013). According to their hypothesis, channel deepening results in tidal amplification, or, more generally, tidal deformation (van Maren et al., 2015). As a result of which fine sediment import increases, leading to a higher SSC. The higher SSC causes turbulence damping and drag reduction, which in turn enhances tidal deformation, hence forming a feedback loop.

A crucial step in their analysis is the impacts of suspended sediment on the effective hydraulic drag, upon which the response of estuaries to narrowing and deepening becomes amplified. By lowering the bed roughness, various (idealised or complex) models reproduced the upstream shift in the ETM position and the transition to high SSC after the channel deepening (Chernetsky et al., 2010; de Jonge et al., 2014; van Maren et al., 2015). These results, however, followed from recalibration. The reduced roughness thus was not resolved by the model itself, and the transition was not dynamically modelled.

Theoretical expressions for the drag coefficient are a function of the

\* Corresponding author.

E-mail address: [qinghe@sklec.ecnu.edu.cn](mailto:qinghe@sklec.ecnu.edu.cn) (Q. He).

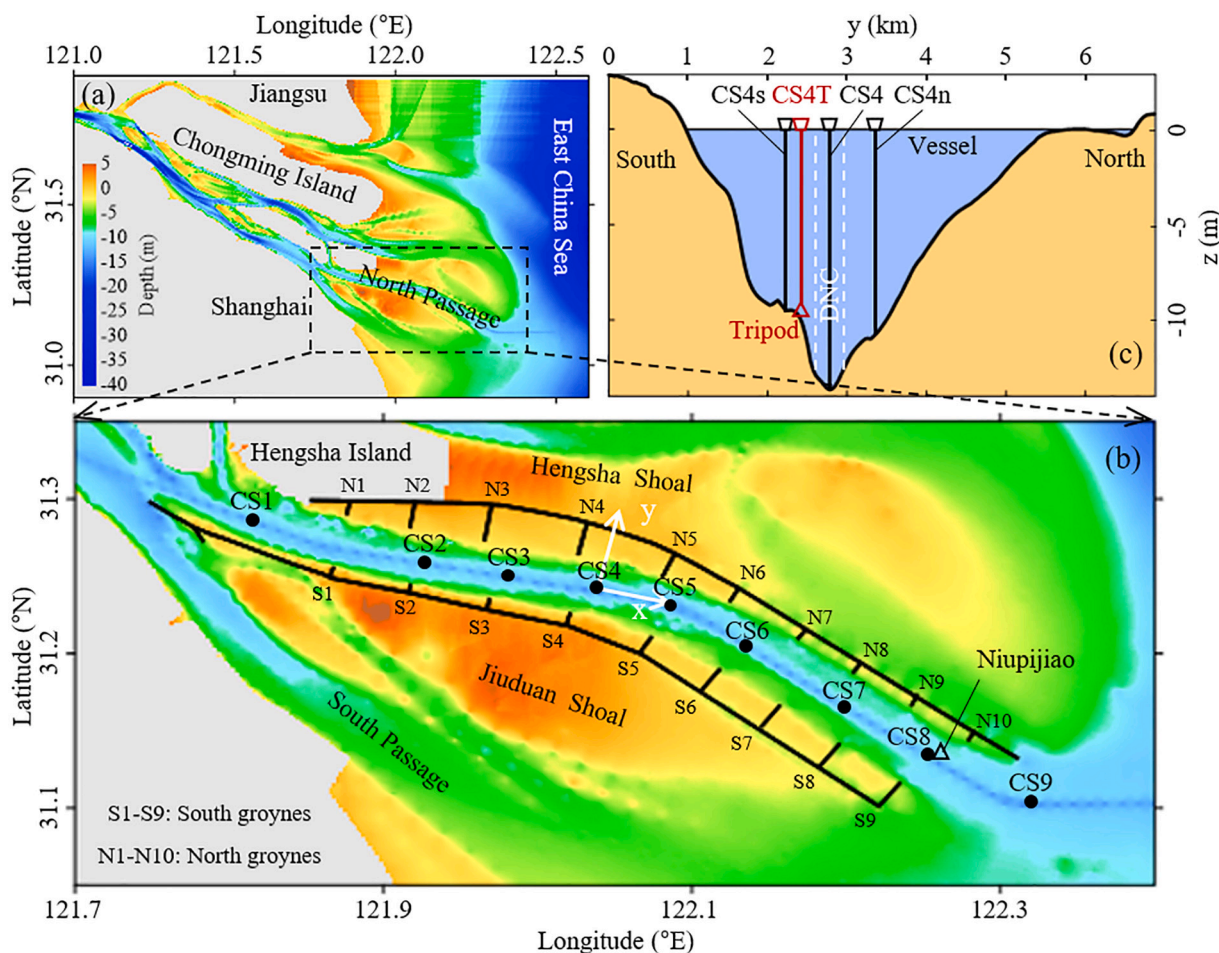


**Fig. 1.** (a) Bathymetry of the Changjiang River Estuary. The water depth is relative to the theoretical depth datum. The dashed box indicates the study area, which is enlarged in Fig. 1b. (b) The Deepwater Navigational Channel (DNC), dykes and groins along the North Passage. The dots represent the ship-borne stations deployed in August 2012. The triangle indicates the tide gauging station located in Niupijiao. The  $x$  and  $y$  coordinates denote the along- and cross-channel direction, respectively. (c) A cross-channel transect at CS4. The black lines represent three ship-borne stations deployed in 2012, and the red line denotes the station in 2014, including ship- and tripod-borne observations. (For interpretation of the references to colour in this figure legend, the reader is referred to the web version of this article.)

(flux) Richardson number (Wang, 2002; Winterwerp et al., 2009). The semi-analytical approach by Winterwerp et al. (2009) was used to analyse the tidal response to river engineering works (Winterwerp and Wang, 2013). Their analyses present a snowball effect between tidal amplification, sediment import and drag reduction. Dijkstra et al. (2019) went one step further and dynamically modelled the transition in SSC by including a reduced drag coefficient in their model. Their results highlight the role of drag reduction in the sediment import capacity of the system and hence the regime shift, supporting the feedback loop proposed by Winterwerp and Wang (2013). In order to reproduce the increase in SSC, Dijkstra et al. (2019) assumed that sediment is efficiently resuspended from the bed. The efficient resuspension was achieved in their model by choosing a high value of erosion parameter and by including hindered settling and excluding the effect of drag reduction on erosion. However, the validity of such an assumption has not been confirmed by observations. Available field observation to date to verify the theoretical expressions for drag reduction is scarce.

Studies mentioned above on the regime shift in estuaries mainly focus on large-scale along-estuary (longitudinal) processes (e.g., tidal deformation and sediment import). Small-scale vertical processes, however, received little attention. The imported sediment may first accumulate near the bed, forming concentrated benthic suspensions (CBS). CBS is defined as a near-bed high-concentration suspension of fine sediment. From a physical perspective, the CBS exhibits notable turbulence damping and hindered settling, but remains Newtonian.

(Winterwerp, 2002; Bruens et al., 2012). Large vertical SSC gradients exist within CBS, leading to turbulence damping through buoyancy effects and hence drag reduction (Winterwerp, 2001; Becker et al., 2018). In suspensions of fine sediment (e.g., Severn Estuary and Changjiang Estuary), hindered settling becomes important when SSC is higher than  $\sim 10 \text{ kg/m}^3$  (Manning et al., 2010; Wan et al., 2015). Rheologic experiments show that the suspension of fine sediment displays Newtonian behaviour for a concentration of  $< 80 \text{ kg/m}^3$  (Wang et al., 1998; Thompson et al., 2006). Therefore, near-bed suspensions of fine sediment with a concentration of  $10\text{--}80 \text{ kg/m}^3$  are considered as CBS in this study.

A positive feedback loop between vertical mixing and settling was proposed for the formation of CBS in estuaries (Winterwerp, 2002; Xu, 2009; Ge et al., 2018). Density stratification, generally initiated by salinity stratification, inhibits vertical mixing through buoyancy destruction (i.e., turbulence damping). Suspended sediment is therefore confined in the bottom layer (Geyer, 1993), leading to decreasing SSC in the upper water columns. Accumulated sediment produces a strong SSC gradient which in turn strengthens stratification and causes further sediment trapping near the bed (Winterwerp, 2001). With increasing SSC, hindered settling becomes essential and provides a favourable situation for near-bed high SSC (Dijkstra et al., 2018). Once CBS forms, such a positive feedback loop favours the stability of CBS. This feedback loop, combined with the one proposed by Winterwerp and Wang (2013) for regime shift in estuarine SSC, may result in the transition in vertical

profiles of SSC. Since sediment tends to accumulate in the bottom layer, SSC near the bottom may increase earlier than near the surface. In other words, the hyper-turbid state develops from the bed to the water surface during the transition. Although CBS was frequently found after channel deepening (Wang, 2010; Becker et al., 2018; Lin et al., 2020), no study to date shows the transition in vertical SSC profiles.

In this study, we focus on the North Passage of the Changjiang (Yangtze River) Estuary (Fig. 1), where a Deepwater Navigational Channel was constructed to meet the demand for sailing traffic. The construction was launched in 1998, and the waterway depth was developed in three phases: (1) to 8.5 m in 2002, (2) to 10 m in 2005 and (3) to 12.5 m in 2010 (Liu et al., 2011). After dredging operations, the ETM shifted 10–15 km upstream and became a wide turbidity zone between CS2 and CS8 (Jiang et al., 2013). The maximum SSC near the bed increased from several to tens kg/m<sup>3</sup> (Jiang et al., 2013; Wan and Zhao, 2017; Lin et al., 2020), although the sediment supply from the Changjiang River declined by 70% (Guo et al., 2019). However, the changes in SSC profiles remain unclear.

The objective of this study is to check whether a transition in SSC profiles occurs in the North Passage and to quantify the drag reduction caused by suspended sediment. This is done by analysing historical SSC observations at the same or nearby sites as well as the near-bottom measurements by a tripod system. An introduction to the Changjiang Estuary is given in Section 2. Section 3 presents the data and methods used in this study. The results are shown in Section 4, including regime shift in SSC profiles, mobile CBS pool, drag reduction and tidal asymmetry. The implications of the results to regime shift and sediment transport in estuaries are discussed in Section 5. Finally, the conclusions are summarised in Section 6.

## 2. Study area

The Changjiang River is one of the largest rivers in the world in term of its river discharge and sediment load. The Datong gauging station, ~640 km upstream from the river mouth, is the tidal wave limit. Here, daily river discharge and sediment load are measured. The annual suspended sediment load at Datong declined from 470 million tons (1953–1985) to 140 million tons (2003–2015) due to soil conservation strategies and dam construction while the mean river discharge is relatively stable (28,200 m<sup>3</sup>/s) (Guo et al., 2019). Both freshwater discharge and sediment load show seasonal variation. The discharge is approximately 40,000 m<sup>3</sup>/s in the wet season (May–October) and ~10,000 m<sup>3</sup>/s in the dry season (November–April) (CWRC, 2014). More than 70% of sediment load is delivered to the estuary in the wet season.

The Changjiang Estuary is partially stratified with moderate tidal forcing. The mean and maximum tidal ranges are approximately 2.7 and 5.0 m, respectively, according to data of the tide gauging located at Niupijiao (Guo et al., 2015). Local mixing and stratification are controlled by tidal currents, saltwater intrusion and freshwater discharge. Local stratification is enhanced with saltwater intrusion. Stronger stratification tends to occur in wet seasons and on neap tides (Pu et al., 2015).

The North Passage of the Changjiang Estuary was deepened and dyked, forming a Deepwater Navigational Channel with a width of 350 m and a depth of 12.5 m (referred to the Theoretical Depth Datum). The construction includes two jetties (each 50 km) and 19 groins. After the construction, the saltwater intrusion is enhanced in the upper reaches and weakened in the lower reaches of the North Passage (Zhu et al., 2006). Before the construction, flows could spill over the shallow shoals at high waters, leading to strong lateral (cross-shoal) flows (Song and Wang, 2013; Zhu et al., 2018). After the work, the jetties partially block lateral flows and inhibit the water and sediment exchanges between the channel and shoals.

**Table 1**

Conditions of the in-situ measurements of suspended sediment concentrations in the North Passage.

Time	Location	Depth (m)	Tidal range (m)	Discharge <sup>a</sup> (m <sup>3</sup> /s)
30–31 Jul. 1988	N31°15.0' , E122°0.5'	7.0	4.4	27,900–43,200
29–30 Jun. 1999	N31°11.5' , E122°8.4'	9.0	3.6	38,200–51,500
19–20 Aug. 2005	N31°14.2' , E122°1.5'	10.2	4.2	36,400–49,800
20–21 Aug. 2009	N31°14.2' , E122°1.5'	11.7	4.1	38,600–44,800
17–18 Aug. 2012	N31°14.2' , E122°1.5'	11.9	4.5	50,700–57,900
14–15 Jul. 2014	N31°13.9' , E122°2.3'	12.1	4.1	34,600–47,100
14–15 Aug. 2015	N31°13.9' , E122°2.3'	11.6	4.0	31,000–49,800

<sup>a</sup> Discharge measured at the Datong gauging station during the observation.

## 3. Data and methods

### 3.1. Historical bathymetry and SSC

Bathymetric data in 1986 and 1997 were digitised from marine charts with an accuracy of ±0.2 m. The data from 2002 to 2016 were measured by echo sounders with an accuracy of ±0.1 m. More details on bathymetric data, refer to Zhu et al. (2019). All bathymetric data were converted to be negative downward relative to the theoretical lowest tidal level.

In-situ SSC measurements from 1988 to 2015 were used to investigate the regime shift in SSC in the North Passage. All data were obtained near the station CS4s (Fig. 1) during the spring tide of wet seasons. Table 1 summarises the conditions during the observations. For each campaign, water samples were hourly collected in six relative-depth layers, i.e.,  $z/H = 0.05$  (near the bed), 0.2, 0.4, 0.6, 0.8 and 0.95 (near the surface), where  $H$  is the water depth, and  $z$  denotes the height above the bed. Each water sample was filtered through a pre-weighed filter (0.45 μm), and the filter was dried at 40 °C for 48 h and reweighed to determine the SSC.

### 3.2. Survey and instruments

In order to capture the CBS and study its effects on the regime shift in SSC, two fieldworks were conducted in the North Passage. Table 2 summarises the instruments employed and their configurations during the observations. All data were collected during the spring tide of wet seasons under calm conditions (no storms). The wind speed was <6 m/s, and the significant wave height was <0.2 m. The discharges, measured at Datong, were ~57,000 m<sup>3</sup>/s and ~44,350 m<sup>3</sup>/s during the observation in 2012 and 2014, respectively.

In August 2012, profiles of velocity, salinity and SSC were simultaneously measured in an along-channel transect with nine stations (CS1, CS2, CS3, CS4, CS5, CS6, CS7, CS8 and CS9; Fig. 1b). The spacings between stations from upstream to downstream are 10.7, 4.1, 4.9, 5.5, 6.8, 6.6, 6.5 and 7.2 km, respectively. Meanwhile, profiles were collected in a cross-channel section with three stations (CS4s, CS4 and CS4n from south to north) (Fig. 1c). The spacing between stations is ~500 m. Flow velocity and direction were obtained by rotor current meter (RCM), and SSC and salinity were derived from water samples. These data were collected every 30 min in the six relative-depth layers. This observation lasted for 13 h, covering a tidal cycle during spring tides.

To access high-resolution profiles of velocity, salinity and SSC near the bed, we deployed a tripod system in July 2014. The tripod system was located at CS4T, ~200 m away from the Deepwater Navigational Channel (Fig. 1c). A downward-looking Acoustic Doppler Current

**Table 2**  
Shipboard and tripod instruments and their sampling configurations.

Time	Carrier	Instrument deployed	Distance above the bed (m)	Sampling interval (min)	Sampling configuration	Survey parameter
201,208	Vessel	RCM	*	30	1 Hz × 30 s	Velocity
		Sampler	*	30	–	Salinity, SSC
201,407	Vessel	ADCP	H-0.5	10	0.5 Hz, cell size: 0.5 m	Velocity profiles
		OBS	*	60	1 Hz × 30 s	Salinity, temperature, and SSC
		LISST	*	60	1 Hz × 30 s	Floc size distribution
201,407	Tripod	ADCP-down	1.0	5	1 Hz × 60 s, cell size: 0.05 m	Velocity profiles
		ADCP-up	1.2	5	0.5 Hz × 60 s, cell size: 0.5 m	upper velocity, wave
		ADV	0.35	10	8 Hz × 90 s	near-bed velocity
		RBR	1.1	5	4 Hz × 60 s	Wave conditions
		CTD	0.35	5	1 Hz × 60 s	Salinity, temperature, and depth
		ASM	0.11–1.06	5	1 Hz × 60 s, cell size: 0.01 m	SSC profiles
		OBS	0.35, 0.55, 1.06	5	1 Hz × 60 s	Salinity, temperature, and SSC

The symbol \* denotes that the instrument was moved from the water surface to the bed, collecting data in six relative-depth layers, i.e.,  $z/H = 0.05$  (near the bed), 0.2, 0.4, 0.6, 0.8 and 0.95 (near the surface), where  $H$  is the water depth, and  $z$  denotes the height above the bed.

Profilers (ADCP-down, 1.0 MHz high-resolution profiler, Nortek AS, Norway) obtained velocities from 0.1 to 0.8 m above the bed (mab hereafter) with a resolution of 0.05 m. An upward-looking ADCP (ADCP-up, 600-kHz, Teledyne RD Instruments) was placed at 1.2 mab to measure the velocity profiles in the upper water column with a cell size of 0.5 m. A downward-looking Acoustic Doppler Velocimeter (ADV, Nortek Vector) measured velocities at 0.35 mab with a sampling frequency of 8 Hz. The ADV worked continuously for 90 s every 10 min. The sensors in the ADV were also used to monitor the heading, pitch and roll state of the tripod. An Argus Surface Meter-IV (ASM) measured turbidity profiles from 0.11 to 1.06 mab at a resolution of 1 cm. To measure turbidity, salinity and temperature near the bed, Optical Backscattering Sensors (OBS, D&A Instruments CO, type: 3A, USA) were placed at 0.35, 0.55 and 1.06 mab, respectively. Ship-borne measurements include profiles of velocity, salinity and turbidity above the tripod measured by ADCP and OBS. Water samples were hourly collected in the six relative-depth layers to calibrate the OBSs and ASM. Upon careful sensor calibration, the ASM- and OBS-derived SSC contain a mean relative error of 25% and 30%, respectively (Lin et al., 2020).

### 3.3. Friction velocity and drag coefficient

Friction velocity ( $u_*$ ) is the linkage between current velocity and bed shear stress. Four methods provide estimates of  $u_*$  by (1) log profile (LP); (2) turbulent kinetic energy (TKE); (3) direct covariance (COV) measurement; and (4) inertial dissipation (ID) utilising the Kolmogorov spectrum (Kim et al., 2000). The estimates from the LP and ID methods contain large bias in the presence of stratification (Friedrichs and Wright, 1997; Kim et al., 2000). Considering the high SSC and the frequent occurrence of stratification in the North Passage, we used the COV and TKE methods to estimate the friction velocity.

The instantaneous velocity data recorded within each burst of the ADV provide estimates of TKE, as

$$TKE = \frac{1}{2} (\overline{u'^2} + \overline{v'^2} + \overline{w'^2}) \quad (1)$$

where  $u'$ ,  $v'$  and  $w'$  are streamwise, transverse and vertical fluctuations of velocity, respectively; the overbars indicate time-averaging over each burst period. Turbulent velocity analysis was systematically conducted by the three-stage-post-processing method (Chanson et al., 2008). Note only ADV data with a high signal-to-noise ratio (>5 dB) and correlation (>70%) were used.

As the ratio of bed shear stress ( $\tau_b = \rho u_*^2$ ) to TKE is constant (Soulsby and Dyer, 1981; Stapleton and Huntley, 1995), the estimate of  $u_*$  from the TKE method is given by

$$u_{*TKE} = (C_1 TKE)^{\frac{1}{2}} \quad (2)$$

where  $C_1$  (~0.20) is a proportionality constant.

For a fully turbulent flow with large Reynolds number ( $\kappa u_* z / \nu \gg 1$ ), the COV method gives estimates of  $u_*$  by

$$u_{*COV} = (-\overline{u'w'} - \overline{v'w'})^{\frac{1}{2}} \quad (3)$$

The effect of SSC on flow resistance or bed shear stress can be evaluated by calculating the drag coefficient ( $C_{D(z)}$ ) and friction coefficient ( $f$ ). The drag coefficient is a parameter used for the conversion between friction velocity and current velocity ( $u_x$ ) at height  $z$  above the bed (Thompson et al., 2006; Burchard et al., 2011; Zhu et al., 2016)

$$C_{D(z)} = \left(\frac{u_*}{u_x}\right)^2 \quad (4)$$

The friction coefficient links depth-averaged velocity ( $u_d$ ) to the friction velocity (Wang et al., 1998) by

$$\frac{f}{8} = \left(\frac{u_*}{u_d}\right)^2 \quad (5)$$

Note that the friction coefficient ( $f$ ) relates to the Chézy bed friction coefficient ( $C$  in  $m^{1/2}/s$ ), Manning coefficient ( $n$ ) and water depth  $H$  as  $\frac{8}{f} = \frac{C^2}{g} = \frac{H^{1/3}}{gn^2}$  (Chow, 1959; Wang et al., 1998; Winterwerp et al., 2009).

### 3.4. Eddy viscosity and diffusivity

The effect of suspended sediment on turbulent mixing can be evaluated by calculating the eddy viscosity ( $\nu_t$ ) and diffusivity ( $k_t$ ). Eddy viscosity is a function of internal stress and vertical velocity gradient (Lu and Lueck, 1999):

$$\nu_t = \frac{-\overline{u'w'} \frac{\partial u}{\partial z} + \overline{v'w'} \frac{\partial v}{\partial z}}{\left(\frac{\partial u}{\partial z}\right)^2 + \left(\frac{\partial v}{\partial z}\right)^2} \quad (6)$$

Since the internal stress was obtained by the ADV, direct estimates of eddy viscosity by Eq. (6) were only available at 0.35 mab. To access the eddy viscosity for the entire water column, we employed the model proposed by Munk and Anderson (1948):

$$\nu_t = \kappa u_* z \left(1 - \frac{z}{H}\right) (1 + 10 Ri)^{-\frac{1}{2}} \quad (7)$$

where  $H$  is the water depth;  $Ri$  is the gradient Richardson number defined as

$$Ri = -\frac{g}{\rho} \frac{\frac{\partial \rho}{\partial z}}{\left(\frac{\partial u}{\partial z}\right)^2 + \left(\frac{\partial v}{\partial z}\right)^2} \quad (8)$$

in which  $\rho$  is the density of sediment-laden flow accounting for the effect of temperature, salinity and suspended sediment. This model was

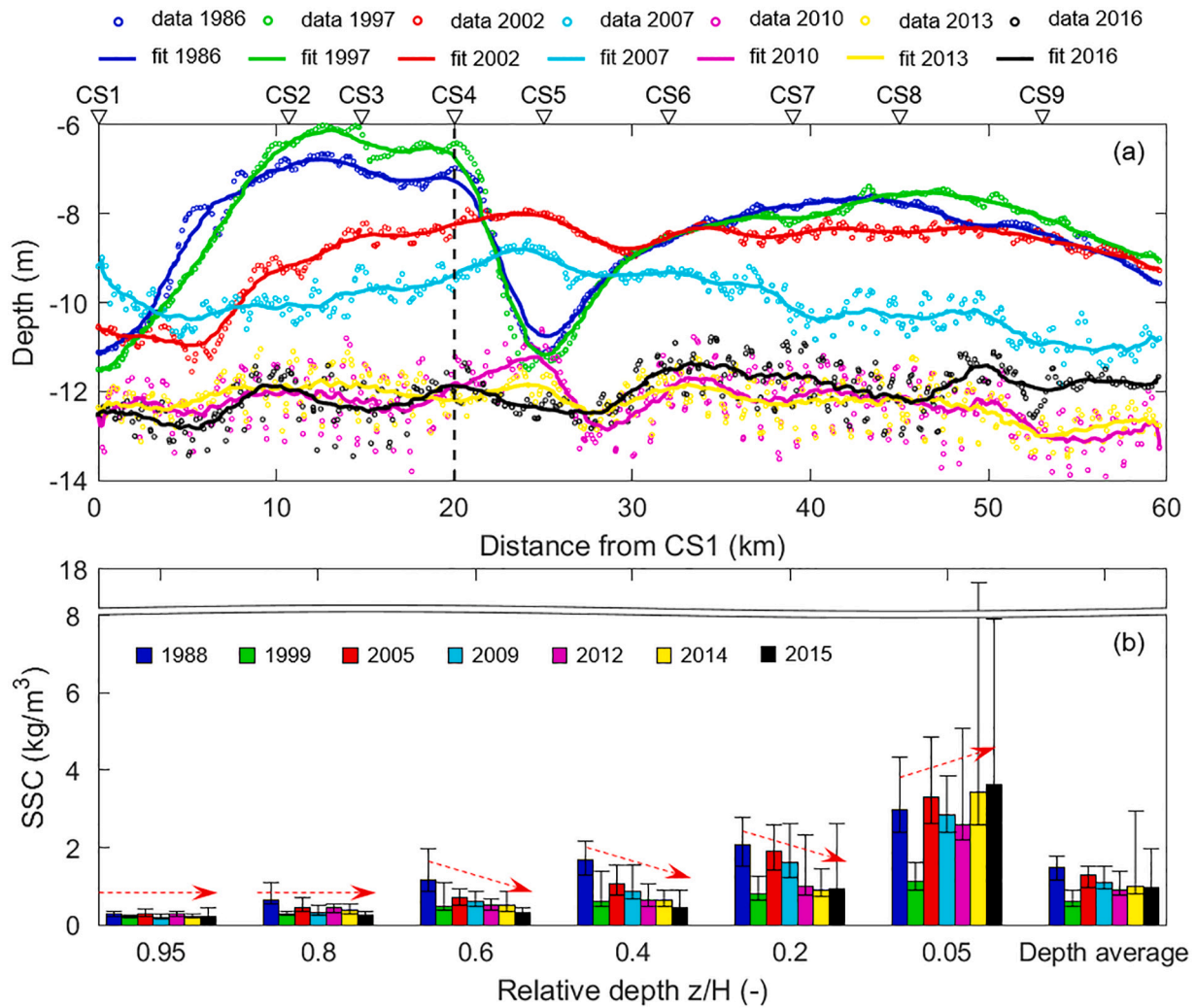


**Fig. 2.** (a) Measured channel depth from 1986 to 2016 with smooth fits. The dashed line indicates the site where historical data of suspended sediment concentrations (SSC) were collected. (b) Tidally averaged SSC in six relative-depth layers, i.e.,  $z/H = 0.05$  (near the bed), 0.2, 0.4, 0.6, 0.8 and 0.95 (near the surface), where  $H$  is the water depth, and  $z$  denotes the height above the bed. Error bars denote standard deviations, and red arrows show the trend in SSC. (For interpretation of the references to colour in this figure legend, the reader is referred to the web version of this article.)

validated against the estimates from Eq. (6) before in-depth analyses.

The turbulent Prandtl–Schmidt number ( $Pr_t$ ) relates eddy viscosity ( $\nu_t$ ) to eddy diffusivity ( $k_t$ ), as  $k_t = \nu_t/Pr_t$ . Since the performance of the standard turbulence model is unsatisfactory in the simulation of sediment diffusion in stratified flow, researchers proposed various parameterisations between  $Pr_t$  and  $Ri$ . Wan and Wang (2017) compared these models and recommended the one proposed by Karimpour and Venayagamoorthy (2014). This model provides reliable estimates by taking the effect of buoyancy and wall boundary into account.

$$Pr_t = \left(1 - \frac{z}{H}\right) \frac{Ri}{R_f} + \left(1 - \frac{z}{H}\right) Pr_{td0} + Pr_{r0} \quad (9)$$

where  $Pr_{td0}$  is the difference between the neutral turbulent Prandtl–Schmidt number at the wall ( $Pr_{tw0} \approx 1.1$ ) and the neutral turbulent Prandtl–Schmidt number for a homogeneous shear flow ( $Pr_{r0} = 0.7$ );  $R_f$  is the flux Richardson number given by  $R_f = 0.25[1 - \exp(-7.5Ri)]$ .

### 3.5. Erosion and deposition

The erosion (entrainment) from the bed (fluid mud layer) to the CBS layer can be determined as follows (Mehta, 1988):

$$E_1 = \begin{cases} M \left( \frac{\tau_b}{\tau_{ce}} - 1 \right) & (\tau_b > \tau_{ce}) \\ 0 & (\tau_b \leq \tau_{ce}) \end{cases} \quad (10)$$

where  $M$  is the bulk erosion coefficient;  $\tau_{ce}$  is the critical shear stress for erosion, with a typical value of  $0.2 \text{ N/m}^2$  in the North Passage (Ge et al., 2015). For simplicity, it is assumed that  $M$  and  $\tau_{ce}$  are uniform over the depth of the sediment on the river bed (i.e., excluding consolidation). Making this assumption has no consequence on our conclusion.

The settling from the CBS to the lower layer can be calculated by

$$D_1 = \omega C_b \quad (11)$$

in which  $C_b$  is the near-bed sediment concentration of the CBS;  $\omega$  is the effective settling velocity, accounting for hindered settling by (Dankers and Winterwerp, 2007)

$$\omega = \omega_0 \frac{(1 - \phi)^2 (1 - \phi_p)}{1 + 2.5\phi} \quad (12)$$

where  $\phi_p = C/\rho_s$  is the volumetric concentration of primary particles;  $\phi = C/C_{gel}$  the relative volumetric concentration. Since near-bed sediment in the North Passage is fine material with a median diameter of  $\sim 12 \mu\text{m}$

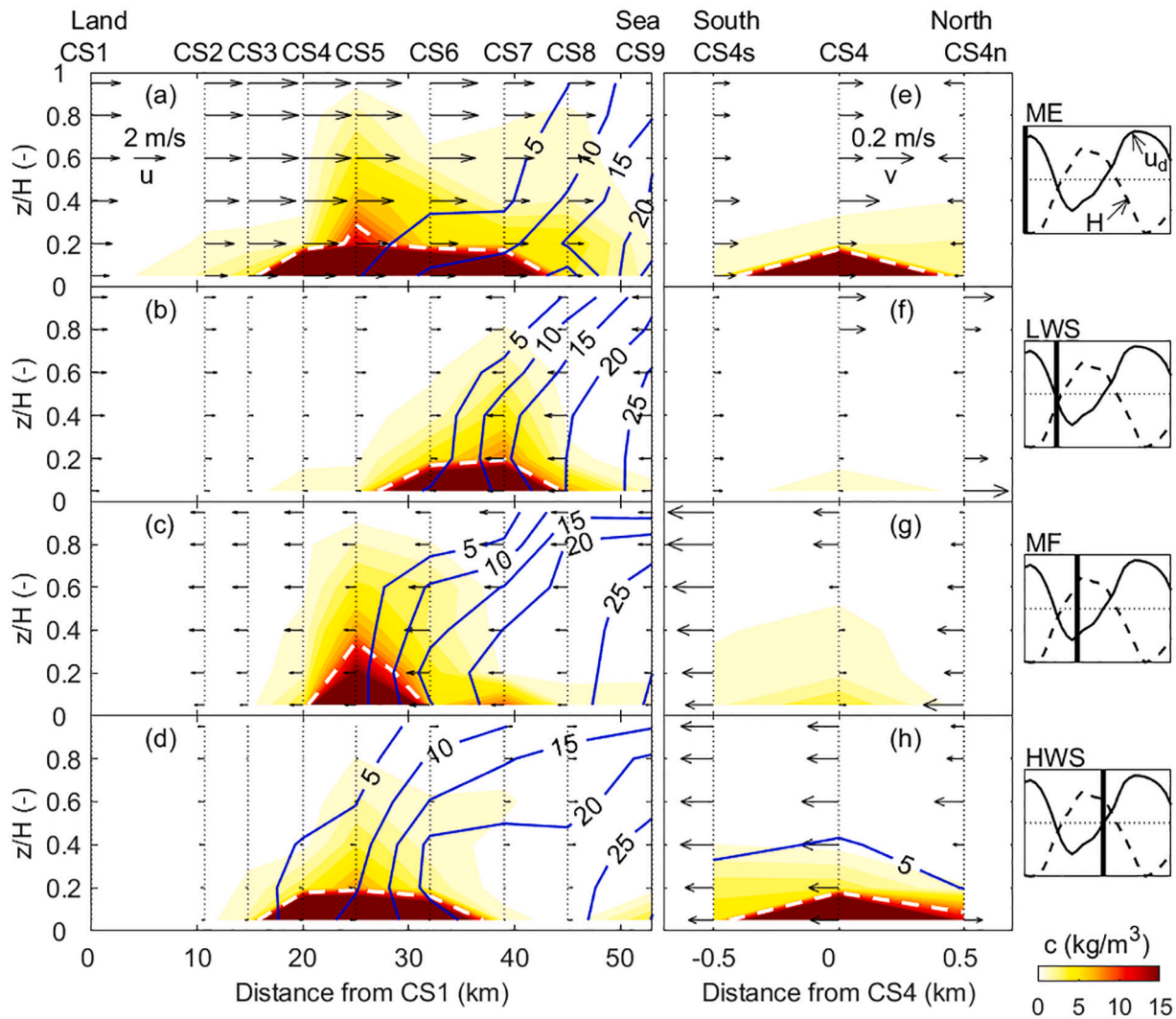


**Fig. 3.** Along-channel (left panels) and cross-channel (middle panels) distributions of velocity (arrows), salinity (contour lines) and suspended sediment concentration (SSC; filled contours) at the time of maximum ebb (ME), low-water slack (LWS), maximum flood (MF) and high-water slack (HWS) during a spring tide (05:00 to 18:00, 17 August 2012). Right panels show the depth-averaged velocity ( $u_d$ ) and water depth ( $H$ ) at station CS4. The white dashed lines denote the contour line of SSC of  $10 \text{ kg/m}^3$ , showing the top of the concentrated benthic suspension. An orthogonal coordinate according to channel direction is used for velocity decomposition. Positive along-channel velocities,  $u$ , at stations CS1, CS2, CS3, CS4, CS5, CS6, CS7, CS8 and CS9 indicate the directions of  $115^\circ$ ,  $101^\circ$ ,  $101^\circ$ ,  $101^\circ$ ,  $113^\circ$ ,  $125^\circ$ ,  $125^\circ$  and  $90^\circ$  from the north, respectively. At each station, positive cross-channel velocity,  $v$ , is perpendicular to  $u$ , pointing from the Jiudian Shoal to the Hengsha Shoal (nearly northward).

(Lin et al., 2020), the gelling concentration ( $C_{gel}$ ) is set to be  $80 \text{ kg/m}^3$  in this study, as observed by Dankers and Winterwerp (2007) in their settling experiments for fine sediment. A sensitivity analysis of the gelling concentration is shown in the Appendix (Fig. A1). When SSC reaches the gelling point, flocs start forming a space-filling network structure on the bed, and the effective settling velocity is zero. In the North Passage, the sediment density ( $\rho_s$ ) is  $2570 \text{ kg/m}^3$  (Guo et al., 2017). The settling velocity of flocs in almost clear water ( $\omega_0$ ) has an average of  $0.1 \text{ mm/s}$  (Wan et al., 2015). Observations by Xu (2009) shows that the bed level near CS4 increases  $\sim 5 \text{ cm}$  after a 3.5-h CBS event. To match this magnitude of bed level variation,  $M$  is set to  $0.001 \text{ kg/m}^2/\text{s}$  in this study.

#### 4. Results

##### 4.1. Regime shifts

The evolution in bathymetry is presented in Fig. 2a, showing a profound deepening between 1997 and 2010. The water depth increased

from  $\sim 6 \text{ m}$  to  $\sim 12 \text{ m}$ . After the Deepwater Navigational Channel Project (2010), the depth is maintained by frequent dredging.

Profiles of SSC near the station CS4 notably changed from 1988 to 2015 (Fig. 2b). Tidally averaged sediment concentrations in the near-surface water column remained stable at a level of  $0.2\text{--}0.3 \text{ kg/m}^3$  ( $0.95H$ ) and  $0.3\text{--}0.6 \text{ kg/m}^3$  ( $0.8H$ ). In the mid-lower water column, concentrations decreased from  $1.2$  to  $0.3 \text{ kg/m}^3$  ( $0.6H$ ), from  $1.7$  to  $0.4 \text{ kg/m}^3$  ( $0.4H$ ) and from  $2.1$  to  $0.9 \text{ kg/m}^3$  ( $0.2H$ ). Observations of near-bed ( $0.95H$ ) SSC, however, show a slight increase from  $3.0$  to  $3.6 \text{ kg/m}^3$ . Although this increase is small, the positive standard deviation significantly enlarged. Enlarged standard deviations in 2014 and 2015 indicate near-bed high concentrations (up to  $40 \text{ kg/m}^3$ ) during the tidal cycle. It suggests that the estuary undergoes a regime shift in SSC profiles as expected, with decreasing SSC in the mid-lower water column and frequent high SSC in the bottom layer.

##### 4.2. Mobile CBS pool

Observations in 2012 show a mobile CBS pool in the mid-lower

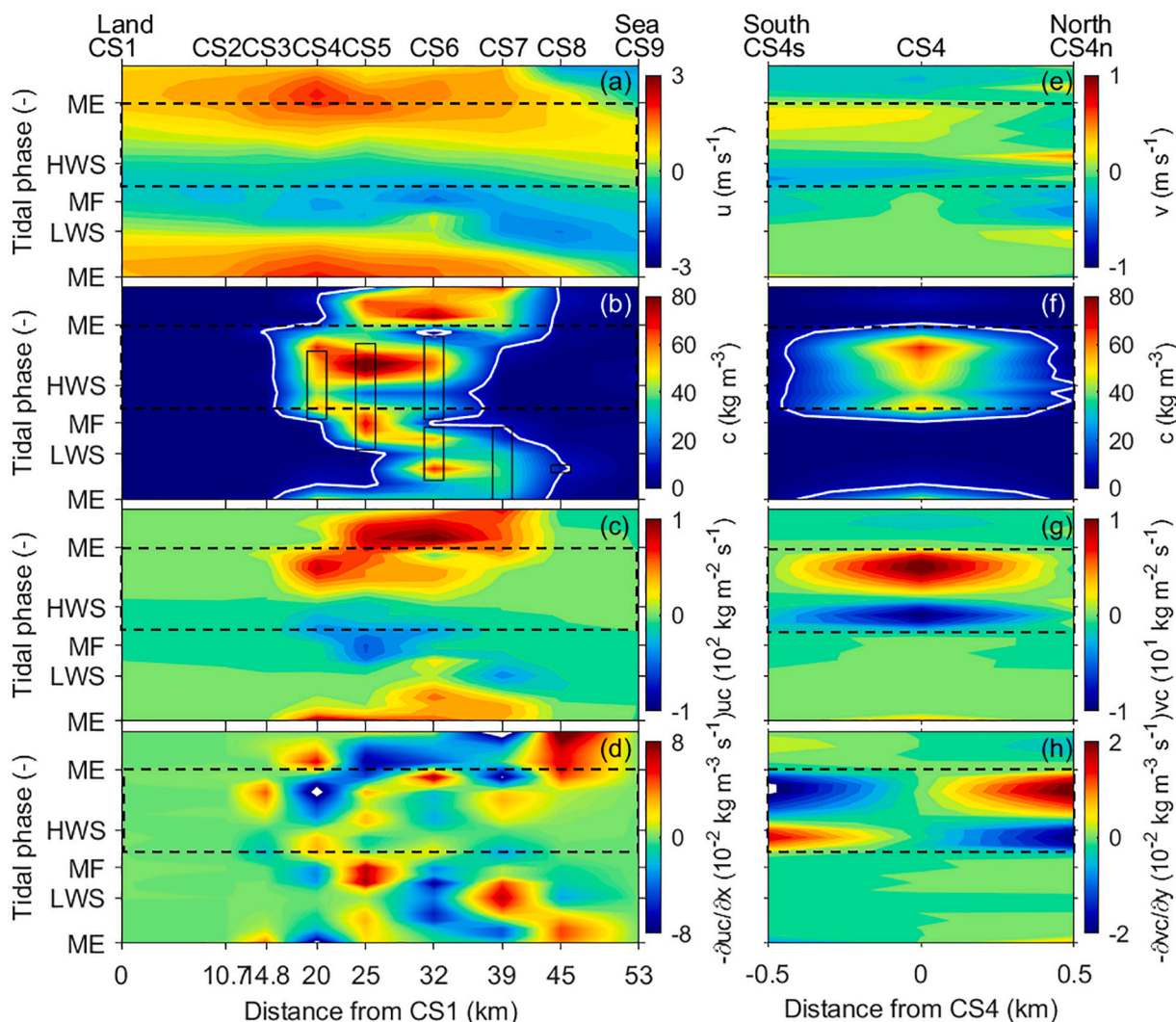


**Fig. 4.** Along-channel (left panels) and cross-channel (right panels) distributions of (a) (e) velocity, (b) (f) suspended sediment concentration (SSC), (c) (g) advective sediment flux and (d) (h) minus the gradient of advective flux in the bottom layer during the spring tide in 2012. Along-channel and cross-channel velocities are represented by  $u$  and  $v$ , respectively. The dashed boxes indicate the period when concentrated benthic suspensions (CBS) occurred at the station CS4. The white lines in panels (b) and (f) show the contour line of SSC of  $10 \text{ kg/m}^3$ . The boxes in panel (b) indicate the period when the net deposition from the CBS to the bed occurred at each station.

reaches of the North Passage (Fig. 3). At low-water slack, the CBS pool was in the lower reaches (between stations CS5 and CS8), with a length of  $\sim 20 \text{ km}$  and a thickness of  $< 3 \text{ m}$ . The pool moved toward upstream then during the flooding tide. At the maximum flood, the pool covered an area from stations CS4 to CS6. The thickness increased and exceeded  $6 \text{ m}$ , while the length reduced to  $\sim 10 \text{ km}$ . At high-water slack, the CBS pool reached CS3, with length and thickness similar to those at low-water slack. On the early ebb, the position of the front of the CBS pool was fixed (at station CS3), although along-channel flows had turned seaward. The tail of the pool, however, retreated directly from high-water slack. As a result, the length of the CBS pool expanded and reached the maximum ( $\sim 30 \text{ km}$ ) at the maximum ebb, covering stations from CS3 to CS8. The thickness at this time was less than  $3 \text{ m}$ , with the maximum at station CS5 ( $\sim 4 \text{ m}$ ). On the late ebb, the CBS pool continued to retreat and back to its initial position at low-water slack. Over a tidal cycle during spring tides, the CBS pool had a mean length of  $\sim 20 \text{ km}$  and a mean thickness of  $\sim 4 \text{ m}$ . At station CS4, the CBS appeared from the maximum flood to the maximum ebb (Fig. 4b).

Cross-channel SSC distributions are presented in Figs. 3e-3h and 4f, showing a limited width of the CBS pool ( $< 1 \text{ km}$ ). The CBS pool mainly exists in the Deepwater Navigational Channel and could not reach the

shallow shoals protected by the groins. The SSC was typically higher in the main channel (up to  $68 \text{ kg/m}^3$ ) than on the flanks ( $< 10 \text{ kg/m}^3$ ). Particularly when the CBS appeared, averaged SSC in the main channel was up to  $50 \text{ kg/m}^3$ , while those on both flanks were  $\sim 3.0 \text{ kg/m}^3$ . Significant lateral SSC gradients were therefore produced. Such considerable gradients, combined with even small lateral flows (averaged  $0.1 \text{ m/s}$ ), could make a crucial contribution to SSC variations on both flanks. From the late flood to the early ebb, southward lateral flows coincided with a sharp SSC increase on the south side and a reduction on the north side of the channel (Fig. 4h). After that, the opposite was true until the maximum ebb. Lateral advection seems to play a vital role in local SSC variations. The CBS events on both sides of the channel may be a result of the cross-channel movements of the CBS pool.

Fig. 5 shows the time series of velocity, salinity and SSC at station CS4T in 2014. Near-surface and near-bed water columns exhibited different intra-tidal variation patterns of SSC. Near the surface, the SSC reached the minimum at slack waters and the peak value at the maximum flood/ebb. It suggests that near-surface SSC was mainly controlled by resuspension and deposition. In the bottom layer, however, high SSC (up to  $63 \text{ kg/m}^3$ ) appeared on the early ebb instead of at the maximum flood/ebb. The CBS was observed only in the lowest  $1 \text{ m}$

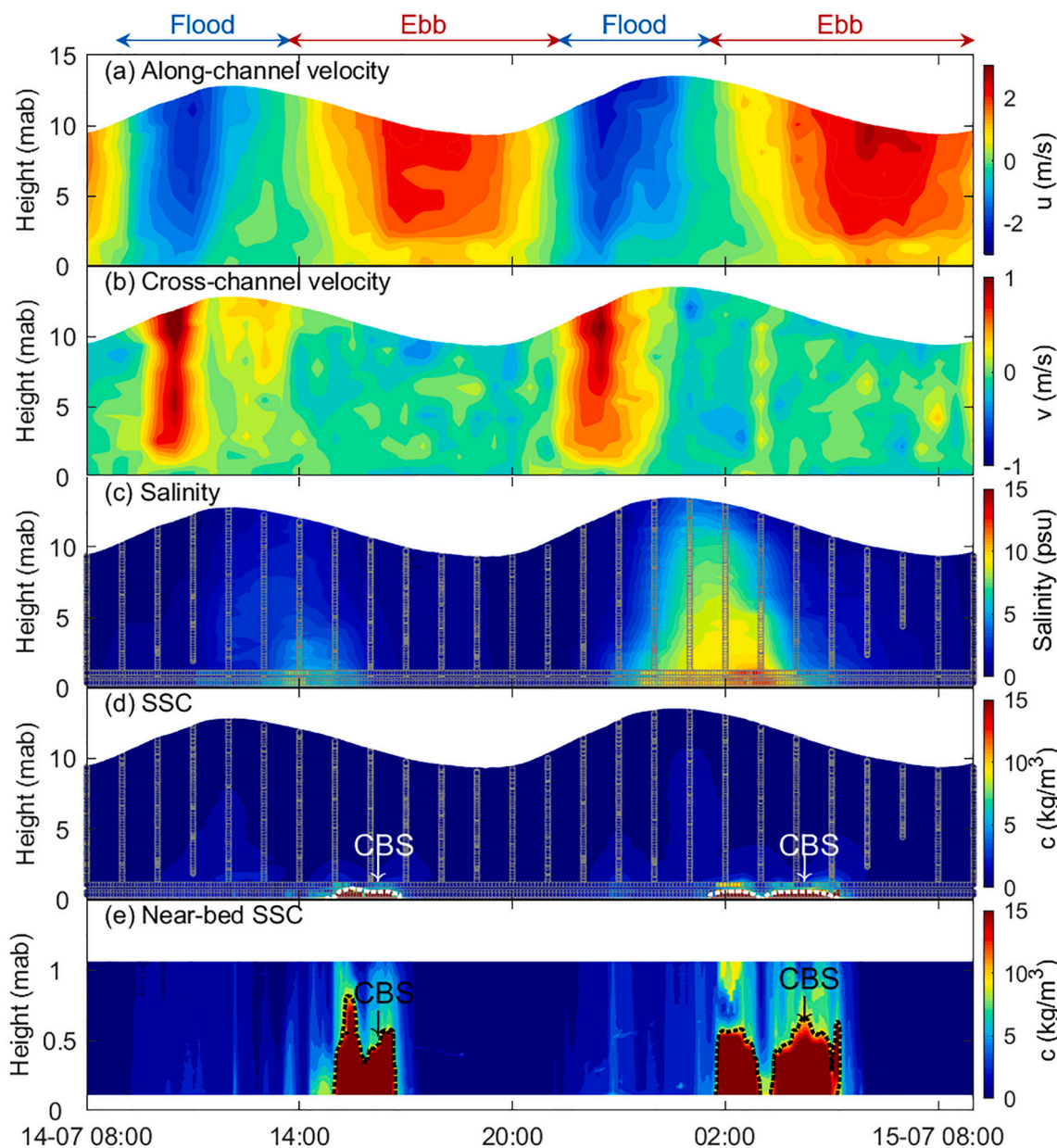


**Fig. 5.** Time series of (a) along-channel velocity ( $u$ ), (b) cross-channel velocity ( $v$ ), (c) salinity, (d) suspended sediment concentration (SSC) and (e) near-bed SSC at CS4T during spring tide. Coloured circles in panels (c) and (d) indicate the valid data collected by instruments. An orthogonal coordinate according to channel direction is used for velocity decomposition. Positive  $u$  and  $v$  denote the direction of  $101^\circ$  and  $11^\circ$  from the north, respectively. The dashed lines show the contour line of SSC of  $10 \text{ kg/m}^3$ , and the CBS represents concentrated benthic suspensions with SSC of  $10\text{--}80 \text{ kg/m}^3$ . The abbreviation ‘mab’ denotes meters above the bed.

from high-water slack to the maximum ebb, with a lifetime of  $\sim 3.5 \text{ h}$  (Fig. 5e). Note the low SSC in the upper water column before CBS events. There was not enough sediment available for settling to support the near-bed high SSC. The CBS at station CS4T, therefore, was not the result of settling from the upper water column.

Near-bed (0.35 mab) variations in SSC and currents are shown in Fig. 6. During the CBS event from 1:40 am to 5:20 am on 15 July, for example, the SSC rapidly increased to the maximum ( $63 \text{ kg/m}^3$ ) in the first 40 min and decreased for the next 60 min. After reaching the minimum ( $\sim 5.0 \text{ kg/m}^3$ ), the SSC increased again (to  $25 \text{ kg/m}^3$ ) and persisted for 80 min, followed by a 30-min reduction. A similar pattern of SSC variation was captured in other CBS events. There were southward lateral flows (from the main channel to the Jiuduan Shoal) during the increase of SSC and northward flows during the reduction (Fig. 6c and d). It suggests that local SSC variation at CS4T is mainly driven by cross-channel flows, as observed in 2012 (Fig. 4h). Southward flows

drive the movements of the CBS pool from the main channel toward the Jiuduan Shoal, leading to the rapid SSC increase at station CS4T, while the return flows cause decreasing SSC. However, the SSC reduction at the end of the CBS event is an exception. This reduction could be attributed to the seaward movement of the CBS pool. During this period, the CBS pool was moving seaward. When the pool moved further downstream, it no longer covered the station CS4T. The SSC at CS4T, therefore, was maintained relatively low on the late ebb.

### 4.3. Drag reduction

Based on turbulent velocities measured at CS4T in 2014, the drag reduction can be quantified. Before the quantification, we compared the estimates of friction velocity ( $u_*$ ) given by the TKE method and COV method. The results show that these two methods give similar estimates (Fig. 7a). The ratio of squared friction velocity to squared depth-

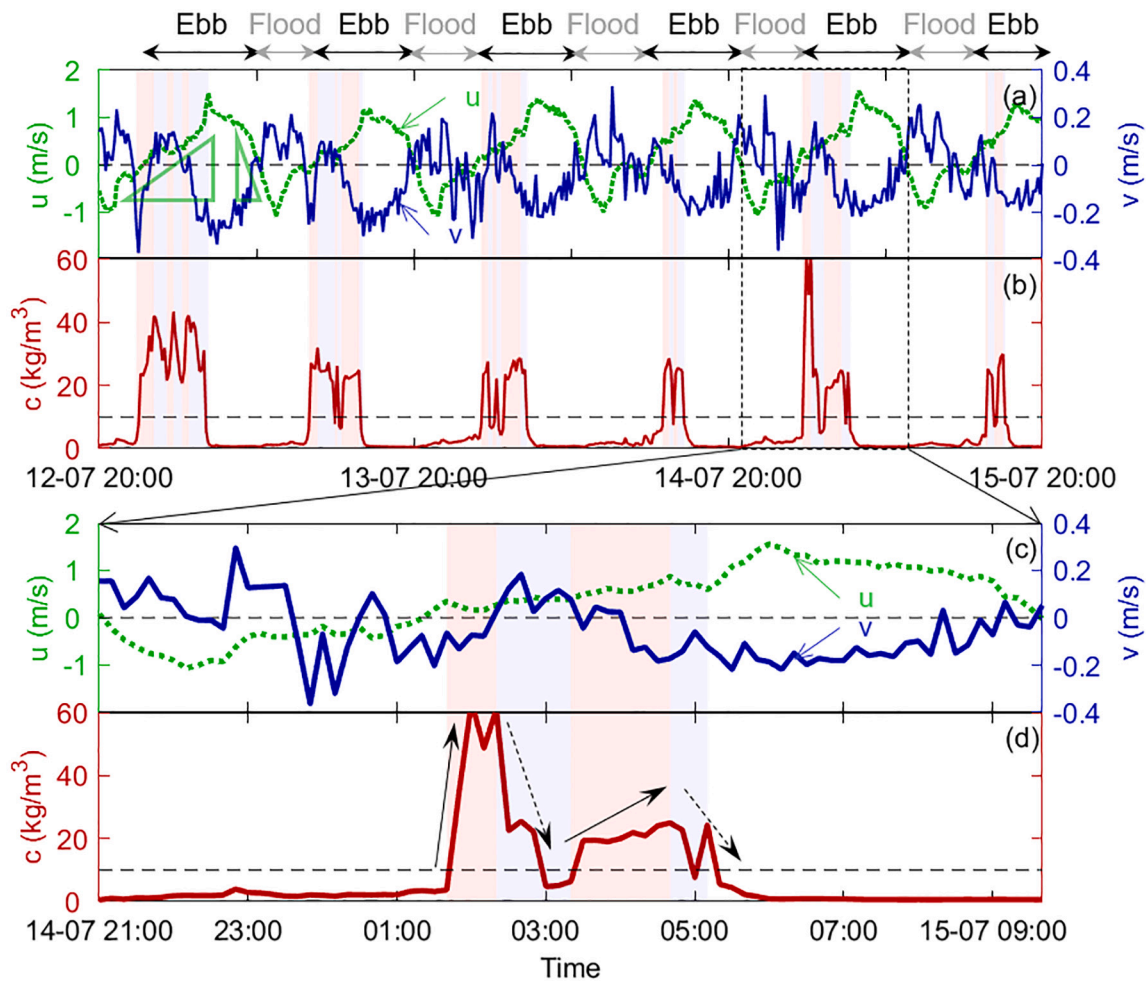


**Fig. 6.** Time series of (a) along-channel ( $u$ ) and cross-channel ( $v$ ) velocity and (b) suspended sediment concentration at 0.35 m above the bed. Panels (c) and (d) show the zoom-in series over a spring tidal cycle from 21:00, 14 July to 09:00, 15 July 2014. Positive  $u$  indicates the ebb direction ( $101^\circ$  from the north), and positive  $v$  represents the nearly northward cross-channel flows ( $11^\circ$  from the north). The triangles (slopes) in panel (a) indicate the slack-water asymmetry. At high-water slack, a lower flow acceleration occurs than at low-water slack.

averaged velocity ( $u_d$ ) returns the friction coefficient ( $f$ ); the ratio of squared friction velocity to squared near-bed (0.35 mab) velocity ( $u_b$ ) returns the coordinated drag coefficient  $C_{D(z=0.35)}$ . The friction coefficient and drag coefficient show a similar intra-tidal variation, with high values at slack waters and low values in the presence of CBS (Fig. 7c). The high values during the ebb-flood transition may result from the shear stress induced by cyclonic spirals at low flow velocities (Wu et al., 2011). In order to avoid the contamination of this nonlinear effect, the data at low flow velocity ( $<0.5$  m/s) was removed in the analyses of drag reduction by suspended sediment.

On the late ebb, when CBS and stratification were absent,  $f$  and  $C_D$  ( $z=0.35$ ) had values of  $3.1 \times 10^{-4}$  and  $7.0 \times 10^{-4}$ , respectively. In the presence of CBS,  $f$  decreased to  $0.9 \times 10^{-4}$  and  $C_{D(z=0.35)}$  declined to  $2.5 \times 10^{-4}$ . It suggests that CBS causes a reduction of 60–80% in bed shear stress for given flow velocity. With the assumed critical stresses for erosion, such a drag reduction will reduce erosion (or entrainment) from the consolidated bed (or fluid mud layer), and hence benefit the net deposition of sediment from the CBS to the layers below.

Both normalized friction coefficient ( $f/f_0$ ) and drag coefficient ( $C_{D(z)}/C_{D(z)0}$ ) show a sharp reduction with increasing SSC (Fig. 8). Within SSC of 0.5–10  $\text{kg/m}^3$ , the friction coefficient linearly decreases; in range of 10–40  $\text{kg/m}^3$ ,  $f$  is relatively constant and minimum (Fig. 8a). The reduction in drag coefficient appears to fall into three ranges: (1) 0.5–3, (2) 3–10 and (3) 10–30  $\text{kg/m}^3$  (Fig. 8b). In the first range, the drag coefficient is constant. A linearly decreasing  $C_{D(z)}$  appears in range 2,

and constant and minimum  $C_{D(z)}$  in range 3. The maximum reduction in  $f$  ( $\sim 80\%$ ) and  $C_{D(z)}$  ( $\sim 60\%$ ) were both observed in the presence of CBS. No fluid mud was observed in this study, so the increase of the drag at higher SSC ( $>100$   $\text{kg/m}^3$ ) could not be confirmed by our observations.

#### 4.4. Reduced eddy diffusivity

The eddy viscosity model proposed by Munk and Anderson (1948) was validated by field observations (Fig. 9a). The correlation coefficient between observed and modelled eddy viscosity is at an excellent score level ( $>0.65$ ). Combined with the formulae for turbulent Prandtl–Schmidt number (Karimpour and Venayagamoorthy, 2014), the model can simulate the eddy diffusivity properly. Based on validated models, we obtained profiles of eddy diffusivity in the water column.

Time series of eddy diffusivity shows a profound reduction in the presence of CBS on the early ebb (Fig. 9c). Although profiles of velocity and salinity were similar, eddy diffusivity was significantly lower with than without CBS, in particular near the bed (Fig. 9d and e). Two mechanisms are responsible for this reduction. First, the drag reduction by CBS returns a lower friction velocity, and thus eddy viscosity reduces. Second, SSC gradients in CBS enhance near-bed stratification, leading to a reduction in eddy diffusivity through buoyancy destruction (Fig. 9b). As a result, vertical sediment diffusion from CBS to the upper water column is suppressed, which provides favourable situations for sediment trapping near the bed. Accumulated sediment, in turn, enhances the

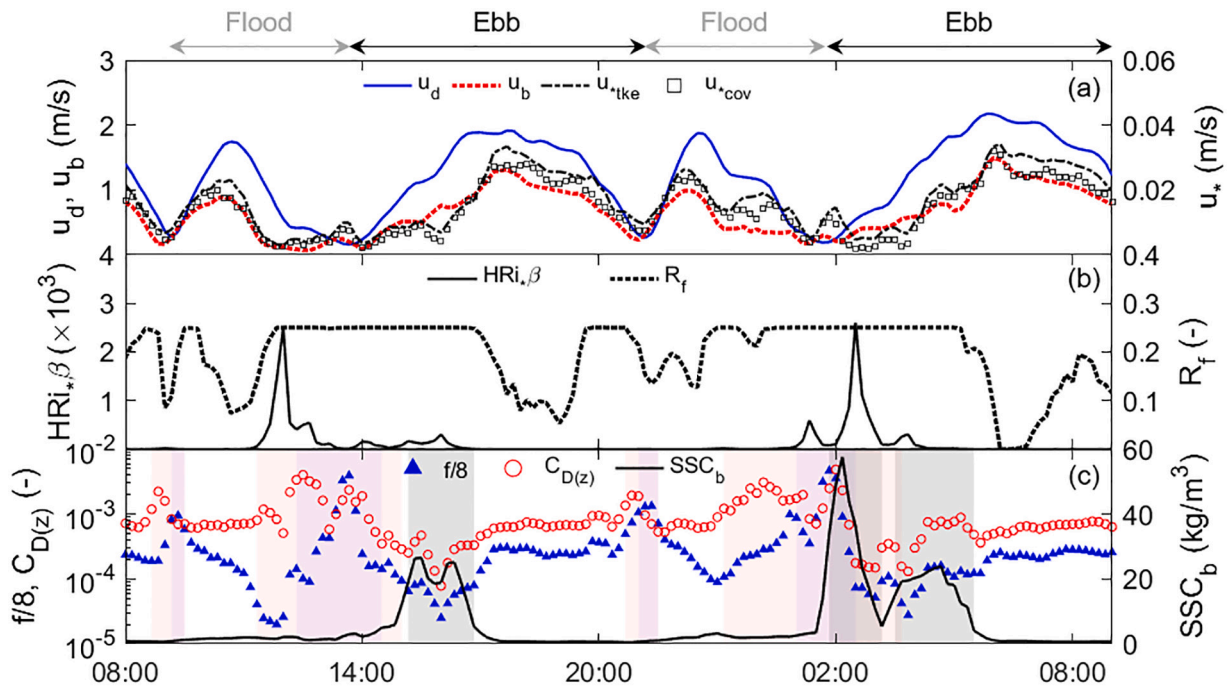


Fig. 7. Time series of (a) depth-averaged velocity ( $u_d$ ), near-bed velocity ( $u_b$ ) and friction velocity given by the TKE method ( $u_{*tke}$ ) and COV method ( $u_{*cov}$ ), (b) near-bed flux Richardson number ( $R_f$ ) and the term  $H Ri_* \beta$  where  $H$  is the water depth,  $Ri_*$  is bulk Richardson number and  $\beta$  is Rouse number, and (c) near-bed suspended sediment concentration ( $SSC_b$ ), friction coefficient ( $f$ ) and drag coefficient ( $C_{D(z)}$ ). The red and blue shadings indicate the periods when  $u_b$  and  $u_d$  are less than 0.5 m/s, respectively. The presence of concentrated benthic suspensions corresponds to grey shading. (For interpretation of the references to colour in this figure legend, the reader is referred to the web version of this article.)

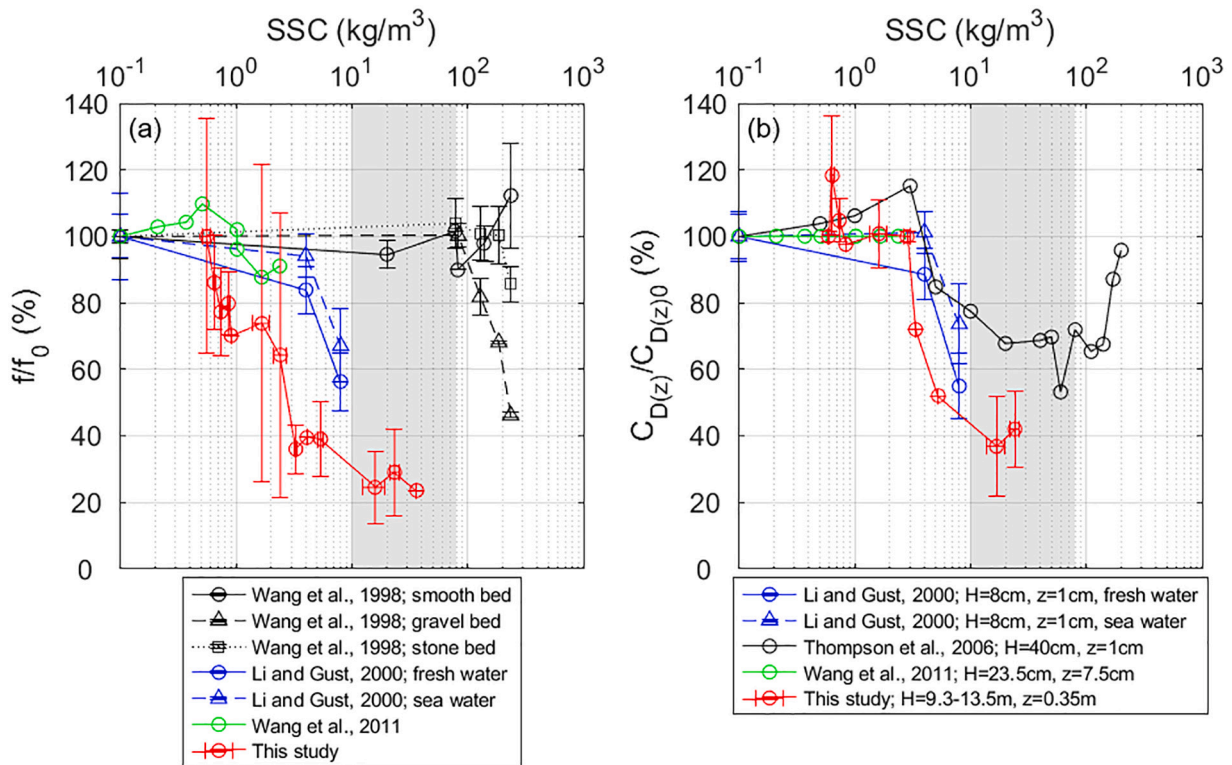
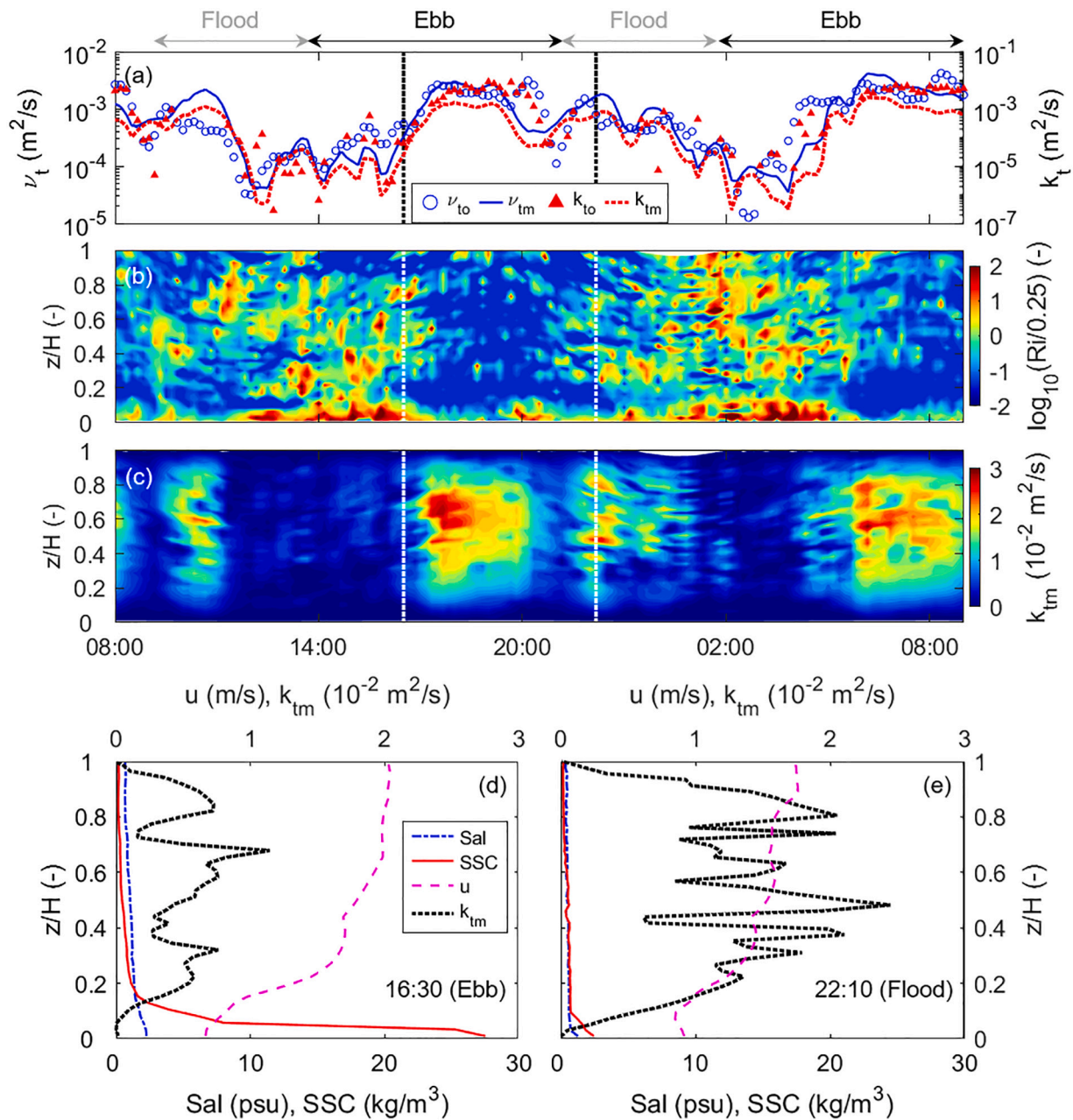


Fig. 8. Normalized (a) friction coefficient ( $f/f_0$ ) and (b) drag coefficient ( $C_{D(z)}/C_{D(z)0}$ ) versus suspended sediment concentration (SSC). The symbols  $f_0$  and  $C_{D(z)0}$  denote the friction coefficient and drag coefficient within the observed lowest SSC. Various types of scatter points represent data from laboratory experiments reported in the literature and field observations (this study). The SSC range of concentrated benthic suspension corresponds to grey shading (Wang et al., 2011).



**Fig. 9.** Time series of (a) observed (scatters) and modelled (lines) near-bed (0.35 m above the bed) eddy viscosity ( $\nu_t$ ) and eddy diffusivity ( $k_t$ ), (b) Richardson number and (c) modelled eddy diffusivity. Typical profiles of velocity, salinity, suspended sediment concentration and eddy diffusivity on the early ebb (d) and early flood (e), showing a reduction in eddy diffusivity in the presence of concentrated benthic suspension.

stability of CBS. These results show indications for the positive feedback mechanisms controlling the formation and maintenance of CBS (Winterwerp, 2002; Ge et al., 2018).

#### 4.5. Tidal asymmetry

The North Passage is ebb-dominant. During the observation in 2012, the depth-averaged velocity of ebb tides was up to 1.8 m/s, while that of flood tides was <1.2 m/s, indicating the asymmetry in peak velocity. Maximum velocity occurred near the water surface and exceeded 3.0 m/s during ebb tides. The duration of the ebb tide was 7.9 h, longer than that of the flood tide (4.5 h). These differences between flood and ebb tides decreased in the bottom layer.

At low-water slack, the flow acceleration is ~2 times higher than at high-water slack (Fig. 10a), indicating the slack-water asymmetry. For a

given critical shear stress for erosion ( $\tau_{ce}$ ) and friction coefficient ( $f$ ), the lower acceleration implies a longer slack (when  $\tau_b < \tau_{ce}$ ) after high water than after low water. Thus, sediment has more time to settle at high-water slack. It suggests that much more intensive deposition occurs at high-water slack than low-water slack. This asymmetry, combined with the movements of the CBS pool (Section 4.2), sheds light on the sediment trapping and channel siltation in the North Passage.

The maximum cross-channel velocity ( $v$ ) was southward and up to 0.4 m/s (Fig. 2). In the bottom layer, the averaged magnitude of southward  $v$  (0.16 m/s) was slightly greater than that of the northward (0.12 m/s). Southward  $v$  occurred for 60% of the time, with the remaining 40% of time northward. These results indicate the lateral flow asymmetry. Strong southward flows persisted from the late flood to the early ebb. As a result, the CBS pool tends to be on the south flank of the channel when reaching the upstream limit, particularly when the net

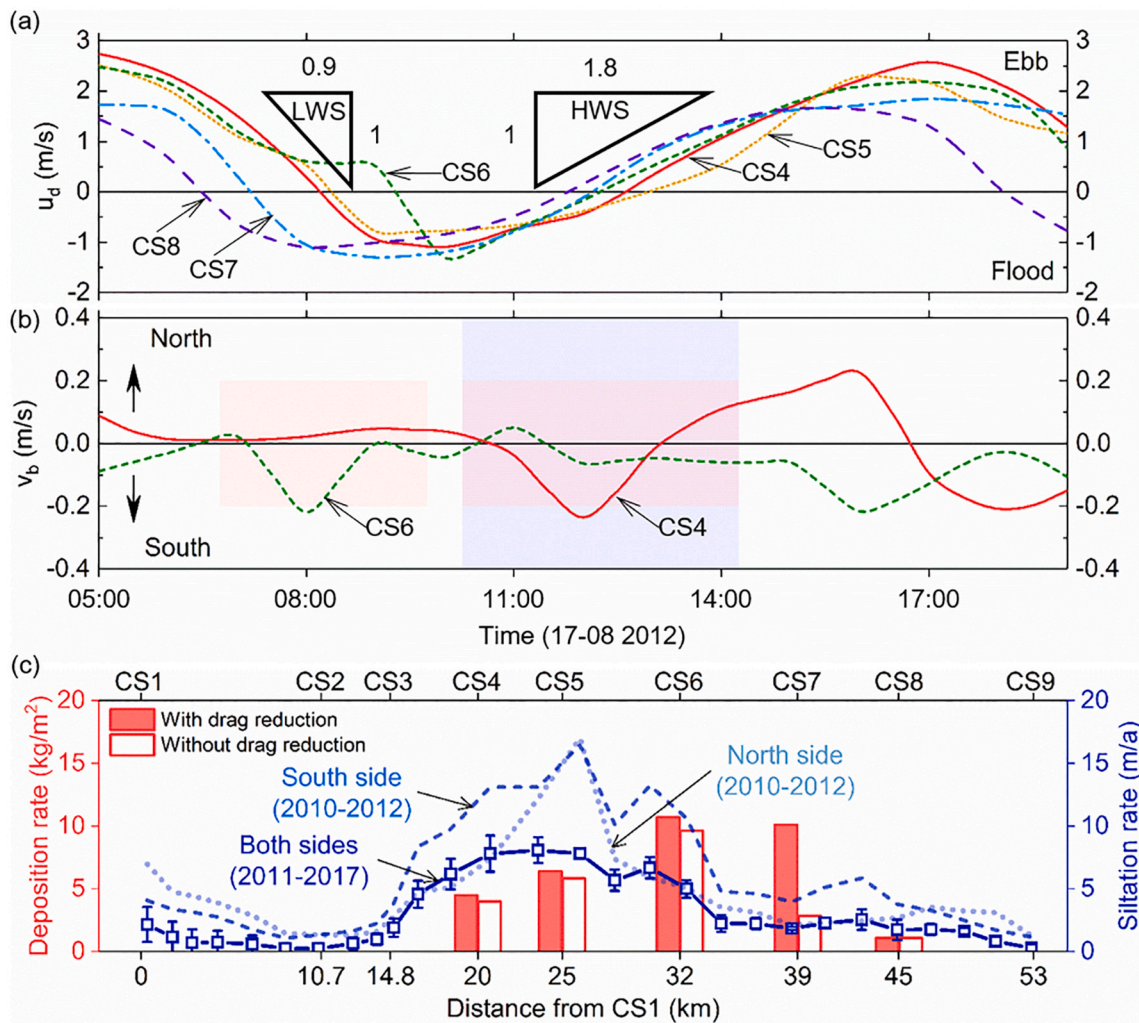


**Fig. 10.** (a) Time series of depth-averaged velocity ( $u_d$ ) at stations CS4, CS5, CS6, CS7 and CS8. Positive  $u_d$  indicates the ebb flow along the channel. The triangles (slopes) show a lower flow acceleration at high-water slack (HWS) than at low-water slack (LWS), i.e. slack-water asymmetry. (b) Time series of near-bed cross-channel velocity ( $v_b$ ) at stations CS4 (solid line) and CS6 (dashed line). Positive  $v_b$  indicates the northward lateral flows from the main channel toward the Hengsha Shoal (Fig. 1). The red and blue shadings indicate the periods when the net deposition of sediment occurred from concentrated benthic suspensions (CBS) to the bed at CS6 and CS4, respectively. (c) Along-channel distribution of yearly siltation rate (lines) in the Deepwater Navigational Channel (data from Liu et al., 2019) and the estimated net deposition rate of sediment from CBS (bars) over the spring tide on 17 August 2012. The filled bars indicate the net deposition rate accounting for CBS-induced drag reduction, while the empty bars do not take drag reduction into account. Note that the siltation rate is the rate of bed level change, whereas the net deposition is the increase of sediment mass on the seabed. They relate to each other through a dry density of 1200 kg/m<sup>3</sup> for dredged sediment (Zhu et al., 2019). (For interpretation of the references to colour in this figure legend, the reader is referred to the web version of this article.)

deposition of sediment occurs from the CBS to the bed (Fig. 10b). The asymmetries in slack waters and lateral flows were confirmed during the observation in 2014 (Figs. 5 and 6).

## 5. Discussion

### 5.1. Field observations vs laboratory experiments

Our field observations show the response of friction coefficient ( $f$ ) and drag coefficient ( $C_{D(z=0.35)}$ ) to SSC (Fig. 8). Both  $f$  and  $C_{D(z=0.35)}$  are relatively constant and minimum within a SSC range of 10–40 kg/m<sup>3</sup> where the CBS occurs, showing a reduction of 60–80% in drag. Within low SSC,  $f$  and  $C_{D(z=0.35)}$  exist different response. The drag coefficient for near-bed velocity ( $C_{D(z=0.35)}$ ) appears constant within the SSC of 0–3 kg/m<sup>3</sup> and linearly decreases in the range of 3–10 kg/m<sup>3</sup>; whereas  $f$ , a friction coefficient for depth-averaged velocity, show a linear decrease in the range of 0–10 kg/m<sup>3</sup>. This difference is due to the height above the bed of the characteristic velocity. In low-concentration sediment-laden flows, near-bed velocity and friction velocity change almost

synchronously with SSC, while the velocity in the upper water column lags. Therefore, near-bed drag coefficient keeps constant in a certain range of SSC, while  $f$  immediately decreases with increasing SSC.

Our results confirm the response of the drag coefficient to SSC observed by Thompson et al. (2006) from laboratory experiments (Fig. 8b). They observed a constant and minimum drag coefficient in the SSC range of 20–120 kg/m<sup>3</sup>, with a reduction of up to 50%. Our field observations, however, suggest a greater drag reduction. The underestimated drag reduction in the lab could be attributed to severe scale effects in small-scale facilities (Winterwerp et al., 2009). In these facilities, the water depth is limited; hence turbulence and mixing are suppressed by the free water surface in addition to sediment concentration. As a result, sediment-induced buoyancy destruction will not be easily observed, and the drag reduction will be underestimated in such small facilities.

### 5.2. Verification of theoretical expressions for drag reduction

The friction/drag coefficient is a function of the (flux) Richardson

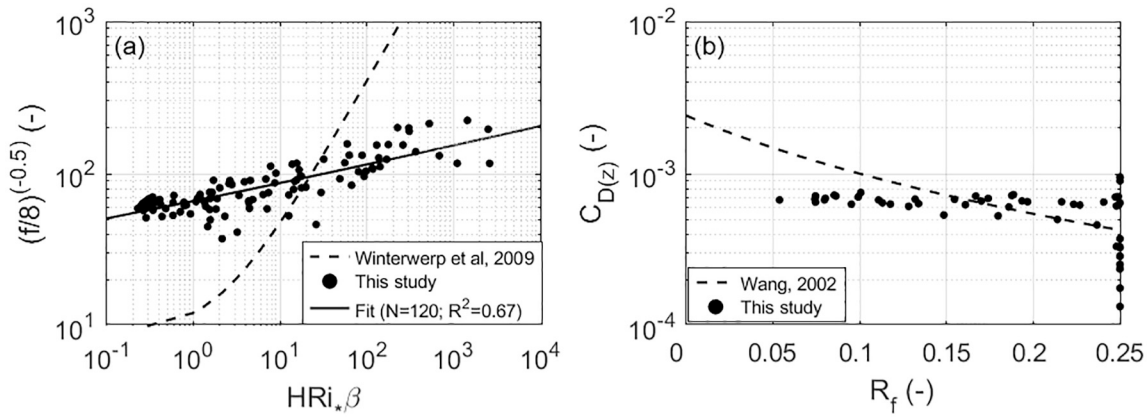


**Fig. 11.** (a) Comparison between observed and modelled friction coefficient ( $f$ ). The horizontal axis is the term  $H Ri_* \beta$  where  $H$  is the water depth,  $Ri_*$  is bulk Richardson number and  $\beta$  is Rouse number. (b) Comparison between observed and modelled drag coefficient ( $C_{D(z)}$ ). The horizontal axis is the near-bed flux Richardson number ( $R_f$ ).

number (Wang, 2002; Winterwerp et al., 2009). Based on the log-linear velocity profile, Winterwerp et al. (2009) derived a simple relation for the friction coefficient (Chézy coefficient in their study) as

$$\left(\frac{8}{f}\right)^{\frac{1}{2}} = \frac{u_d}{u_*} = \frac{C_{eff}}{g^{\frac{1}{2}}} = \frac{C_0}{g^{\frac{1}{2}}} + K_1 H Ri_* \beta \quad (13)$$

where  $C_{eff}$  denotes the effective Chézy coefficient,  $C_0$  is the Chézy coefficient for neutral conditions, and  $Ri_*$  and  $\beta$  are a bulk Richardson number and the Rouse number, respectively, defined as.

$$Ri_* = \frac{(\rho - \rho_w)gH}{\rho u_*^2} \text{ and } \beta = \frac{Pr_* \omega}{\kappa u_*} \quad (14)$$

where  $\rho_w$  is the density of water determined by the equation of state. The

Chézy coefficient for neutral conditions equals to  $25 \text{ m}^{1/2}/\text{s}$  in the Changjiang Estuary (Winterwerp et al., 2009).

The bottom drag coefficient in a sediment-laden bottom boundary layer can be given by (Wang, 2002)

$$C_{D(z)} = \left[ \frac{1 + AR_f \ln \frac{z}{z_0}}{\kappa} \right]^{-2} \quad (15)$$

in which  $z_0$  is the bottom roughness set equal to  $0.1 \text{ mm}$  for the bed sediment in the North Passage with a median grain size of  $12 \mu\text{m}$  (Cheng, 2015; Lin et al., 2020). The effect of stratification is taken into account by a stability function  $(1 + AR_f)$ , where  $A$  is an empirical constant and  $A = 5.5$  for partially stratified estuaries (Wang, 2002).

Our observations could be used to verify these theoretical expres-

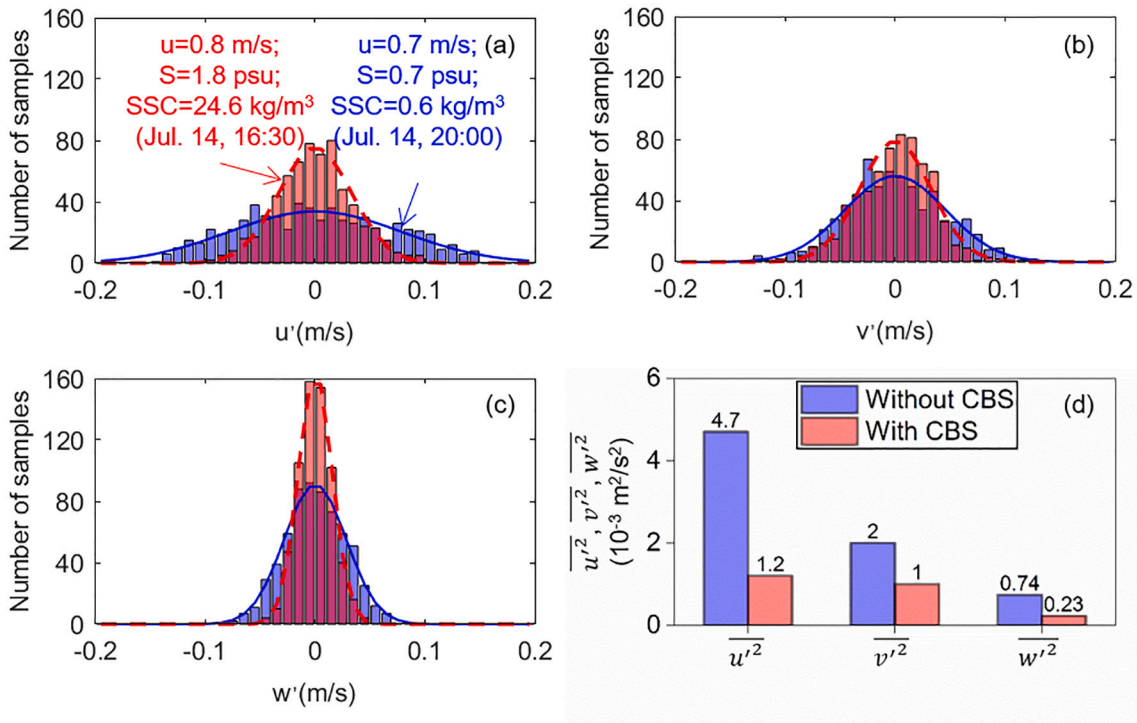


**Fig. 12.** Typical distributions of (a) streamwise ( $u'$ ), (b) transverse ( $v'$ ) and (c) vertical ( $w'$ ) fluctuations of velocity and their Gaussian fits (curves) with (red) and without (blue) the presence of concentrated benthic suspension. (d) Comparison between the burst-averaged fluctuations under these two conditions. Data were collected at CS4T during the spring tide on 14 July 2014. PSU: practical salinity units. (For interpretation of the references to colour in this figure legend, the reader is referred to the web version of this article.)

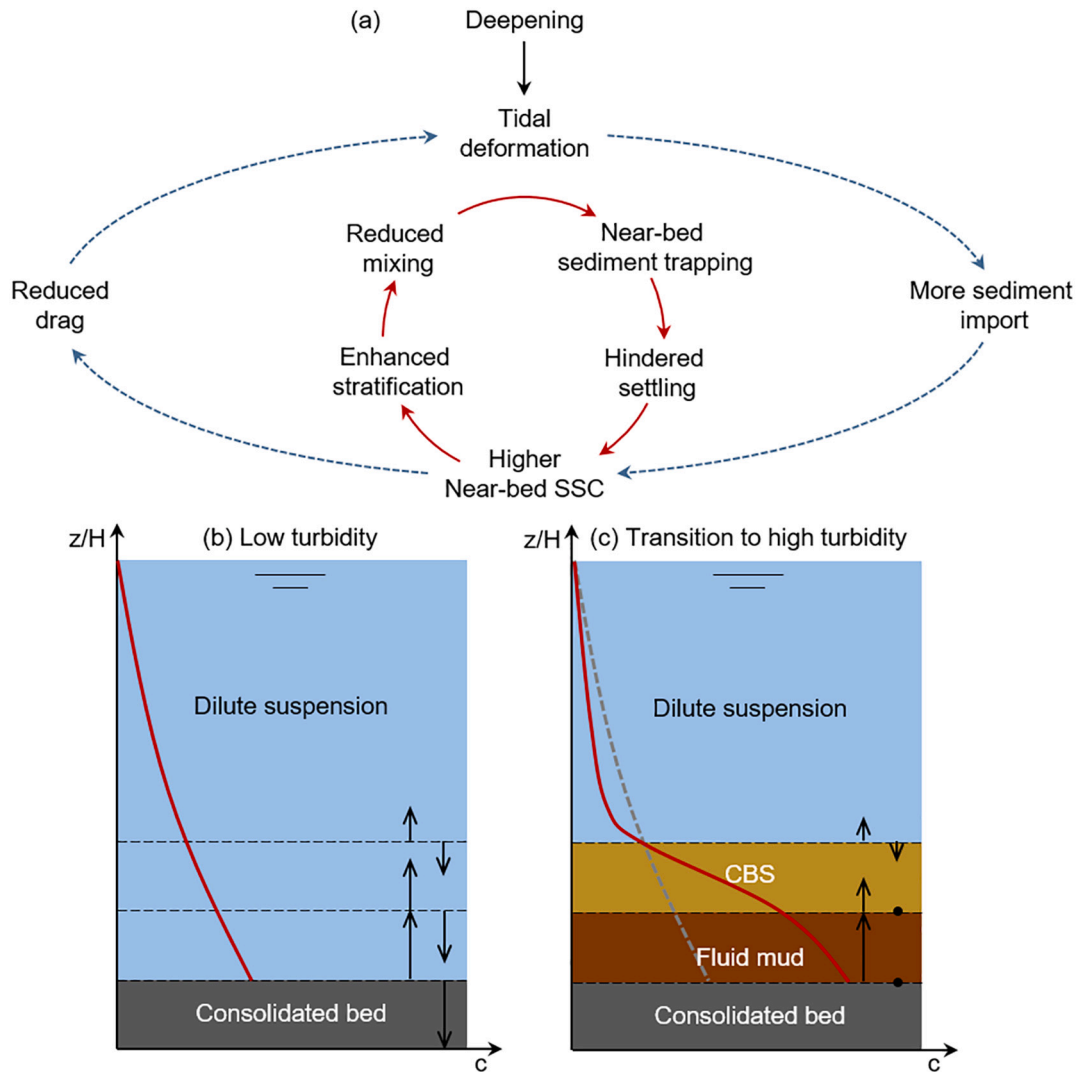


**Fig. 13.** (a) Sketch of the feedback processes underlies a regime shift from low-turbid to hyper-turbid conditions as a consequence of deepening. The feedback mechanism combines the positive feedback loop (dashed blue circle) by Winterwerp and Wang (2013) and Van Maren et al. (2015) and a positive feedback loop of vertical processes (solid red circle). Schematic diagram showing the states of entrainment/erosion (upward arrows) and settling (downward arrows) before (b) and after (c) deepening, explaining the transition in profiles of suspended sediment concentration (SSC, red lines). The length of the arrows scales the magnitude of sediment flux. Under highly turbid conditions, the entrainment and settling reduce due to the turbulence damping and hindered settling, respectively. The erosion of the bed is similar to that under low-turbid conditions as no drag reduction occurs in the presence of fluid mud. The SSC profile in panel (b) is duplicated in panel (c) by a grey dashed line. CBS: concentrated benthic suspensions. (For interpretation of the references to colour in this figure legend, the reader is referred to the web version of this article.)

sions (Fig. 11). The expression by Winterwerp et al. (2009) returns overestimated  $f$  at low Richardson number (low SSC) and underestimated  $f$  at high Richardson number (high SSC). The drag reduction is thus underestimated at low SSC and overestimated at high SSC. The underestimation may be attributed to the fact that this expression does not account for the drag reduction caused by flocculation (Wang et al., 1998), bedforms (Winterwerp et al., 2009) and thickening of the viscous sub-layer (Li and Gust, 2000). The overestimation, however, may result from increasing viscous resistance at high SSC (Wang et al., 1998; Thompson et al., 2006). Our data show a power function relationship between the friction coefficient, the Richardson and Rouse Numbers. An empirical expression is obtained by fitting, as

$$\left(\frac{8}{f}\right)^{\frac{1}{2}} = \frac{C_0}{g^{\frac{1}{2}}} + 58.21(HRi + \beta)^{0.13} \quad (16)$$

with a correlation coefficient ( $R^2$ ) of 0.67 ( $N = 120$ ). Note that this empirical formula only applies to concentrations less than  $40 \text{ kg/m}^3$  and

that viscous resistance needs to be considered at higher concentrations.

The expression by Wang (2002) assumes that  $R_f$  asymptotes to a value of 0.25 around  $Ri \approx 1$  (Mellor and Yamada, 1974; Wang, 2002; Karimpour and Venayagamoorthy, 2014). It means that the turbulence is entirely suppressed by the stratification when  $Ri > 1$ , returning the minimum bottom drag coefficient. Thus, this expression mainly estimates drag reduction when  $Ri < 1$ . Our observations, however, show that the drag coefficient is relatively stable at low Richardson numbers and that a notable drag reduction occurs at higher Richardson numbers ( $Ri > 1$ ) with high SSC (Fig. 11b). It indicates that Eq. (15) underestimates the drag reduction at high sediment concentration, giving an overestimated drag coefficient.

### 5.3. Transition in SSC profiles

Both field observations (Fig. 8) and laboratory experiments (Thompson et al., 2006) show that the maximum drag reduction occurs in the presence of CBS. Such a reduction (up to 60–80%) results from the

turbulence damping. Fig. 12 shows a decrease in velocity fluctuations and TKE in the presence of CBS when compared to values without CBS. Eddy diffusivity, therefore, decreases because of (1) reduced friction velocity (i.e., reduced turbulence production from the bed) and (2) increased buoyancy destruction. As a result, sediment entrainment significantly reduces. On the one hand, reduced entrainment from CBS to upper dilute suspensions decreases the SSC in the upper water column. On the other hand, reduced entrainment favours sediment trapping in CBS and lower fluid mud layers. With sediment accumulation, near-bed SSC increases, hence hindered settling becomes important; and in turn hindered settling supports high SSC by reducing settling from CBS to lower fluid mud layer or consolidated bed (Dijkstra et al., 2018).

No fluid mud and relevant friction/drag coefficient were obtained from our measurements. Results from laboratory flumes (Wang et al., 1998; Thompson et al., 2006) show that the drag in the presence of fluid mud is close to that in clear water (i.e., no drag reduction). This is because, as SSC further increases, viscosity effects begin to outweigh the drag reduction by turbulence damping. It implies that there is no reduction in bed shear stress when fluid mud occurs; hence the erosion from the bed is similar to that under the clear-water condition. Besides, the SSC of fluid mud often exceeds the gelling concentration, so the settling velocity/flux is almost zero. The drainage and consolidation of fluid mud require a long time of slack water, which is hard to achieve in tidal estuaries. Entrainment processes re-fluidise the mud on accelerating tides, preventing the consolidation of the sediment-water mixture (Bruens et al., 2012). As a result, both increased drag and hindered settling favour all erodible sediment to suspend, supporting the assumption by Dijkstra et al. (2019) that the erosion is independent of near-bed stratification. With this assumption, they provided model support for the regime shift in estuarine SSC.

Above analyses suggest a transition of SSC profiles for the regime shift. Our observations provide evidence for the positive feedback loop proposed by Winterwerp and Wang (2013). After the deepening, a mobile CBS pool develops in the North Passage, leading to a drag reduction up to 60–80%. Reduced hydraulic drag strengthens tidal deformation, which may increase sediment import (Xing, 2016). Regarding vertical processes, the erosion of the bed is similar to that under low-turbid conditions as the drag reduction by turbulence damping is counterbalanced by increasing viscosity in the presence of fluid mud. The entrainment of fluid mud and CBS, however, significantly decrease due to the reduction in eddy viscosity by (1) reduced initial turbulence production from the bed and (2) increased buoyancy destruction. Besides, hindered settling support the stability of CBS and fluid mud. As a result, CBS and fluid mud layers develop near the bed, whereas concentrations in the upper water column decrease. A more comprehensive feedback mechanism is sketched in Fig. 13, depicting the transition in SSC profiles during the regime shift to the hyper-turbid state. Such a transition was observed in the North Passage (Fig. 2). Although the decrease in sediment supply from the Changjiang River could also decrease the SSC in the water column (Guo et al., 2019), the frequent high concentrations in the bottom layer confirm this transition in SSC profiles.

#### 5.4. Implications for sediment transport

After the deepening, the North Passage exists a mobile CBS pool. The length and thickness of this pool vary with tidal phases (Fig. 3). These variations imply the development (i.e., formation and breakdown) of the CBS, controlled by the sediment availability from the upper water column and the lower fluid mud layer or river bed. When tidal currents are strong, sediment resuspension and entrainment increase due to strong turbulent shears (Bruens et al., 2012). Strong stratification (generally triggered by salinity), however, inhibits the sediment mixing to the upper water column (Ge et al., 2018). As a result, suspended sediment accumulates near the bottom, leading to the formation of CBS and hence

increasing the thickness of the CBS pool. The accumulated sediment produces strong SSC gradients, which in turn enhances stratification and near-bed sediment trapping (Winterwerp, 2001; Becker et al., 2018). Such positive feedback provides a favourable situation for the formation and maintenance of CBS.

A broader CBS pool occurs at the maximum ebb than at the maximum flood (Fig. 3a and c), which can be explained by stronger stratification on ebb than flood tides (Pu et al., 2015). As the turbulent mixing overcomes the relatively weak stratification on flood tides, sediment can be mixed higher up into the water (Burchard et al., 2018), resulting in an increased thickness of the CBS pool. Once the amount of sediment transported upward is higher than that available from the bed or fluid mud layer, CBS will break down. As a result, the CBS pool is shortest (~10 km) and thickest (~6 m) at the maximum flood. Stronger stratification at the maximum ebb, however, inhibits vertical mixing and confines sediment in the bottom layer (Geyer, 1993), producing CBS. Hence, the longest (~30 km) CBS pool appears, but its thickness is less than that at the maximum flood. The difference of CBS pool between the maximum ebb and the maximum flood confirms the entrainment asymmetry observed by Becker et al. (2018).

At slack waters, both floc size and settling velocity enlarge because of low turbulent shears (Guo et al., 2017). The settling flux of sediment thus increases, lowering the SSC in the upper water column and the thickness of CBS (Fig. 3b and d). However, hindered settling allows for the maintenance of CBS (Dijkstra et al., 2018). The typical settling velocity in the North Passage is ~0.1 mm/s (Wan et al., 2015). For the gelling concentration of 80 kg/m<sup>3</sup> and the mean SSC (28 kg/m<sup>3</sup>) of CBS, the effective settling velocity is ~80% lower and less than 0.02 mm/s. The settling from the CBS to the lower fluid mud or bed is thus inhibited, favouring the stability of CBS.

Our observations show along-channel and cross-channel movements of the CBS pool during the spring tide. The pool is located between CS5 and CS8 at low-water slack and between CS3 and CS7 at high-water slack. During the flood tide, the excursion of the pool is ~10 km, which is consistent with that of saltwater intrusion. The CBS is mainly distributed in the Deepwater Navigational Channel, and the width of the CBS pool is generally less than 1 km. Driven by lateral flows, CBS moves toward the northern shoals on flood tides and the southern shoals on ebb tides. However, the distance of cross-channel movement is limited due to the small amplitude of lateral flows. Thus, the CBS pool could not reach the shallow shoals protected by the groins. Ge et al. (2018) investigated the formation and breakdown of the CBS on the flanks of the channel by a one-dimensional vertical model. However, we argue that the CBS they observed may result from lateral movements of the CBS pool. High SSC driven by lateral flows from the channel was also observed by Li et al. (2019), although no CBS was detected in their study.

The movements of the CBS pool, together with tidal asymmetry (e.g., slack-water asymmetry and lateral flow asymmetry), shed light on the sediment trapping in the estuary. The slack-water asymmetry in the North Passage suggests a longer slack (when  $\tau_b < \tau_{ce}$ ) after high water than after low water (Fig. 10a). Much more sediment thus settles from the CBS to the bed during high-water slack (in the middle reaches) than during low-water slack (in the lower reaches). Such along-channel asymmetry in sediment deposition could be amplified when CBS-induced drag reduction is taken into account (Fig. 10c). Note that the longer slack also favours the consolidation of deposited sediment, which increases the critical shear stress for resuspension and reduces the sediment erosion during subsequent tidal acceleration. Hence, consolidation accelerates the sediment trapping in the middle reaches of the North Passage. Note that our calculations did not account for the dependence of settling velocity on salinity (Fig. 10c). However, flocculation tests suggest that salinity effect favours the sediment trapping in the middle reaches of North Passage, as the salinity there is within the most favourable range (8–13 psu) for flocculation (Wan et al., 2015).

The lateral flow asymmetry in the North Passage results from lateral

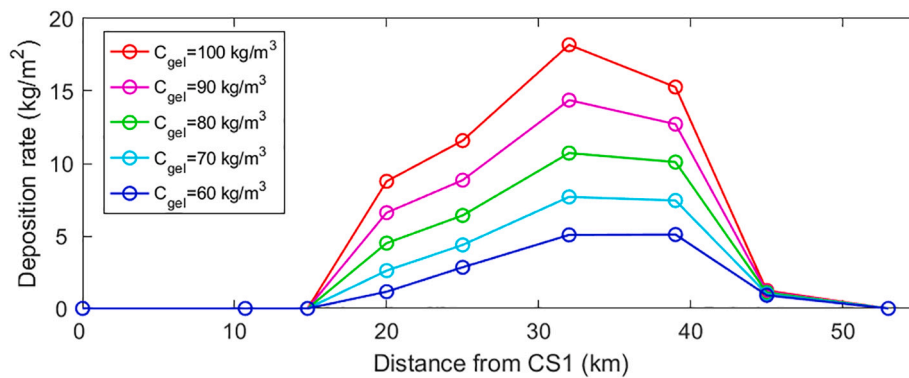


**Fig. A1.** Along-channel distribution of estimated net deposition rate of sediment from CBS over a tidal cycle during spring tide, with different choices of gelling concentration ( $C_{gel}$ ).

density gradients and the curvature effect (Chen and de Swart, 2018; Zhu et al., 2018; Zhou et al., 2019). Due to the lateral flow asymmetry, the CBS pool tends to move to the south flank of the channel, especially when sediment settles from the CBS to the bed (Fig. 10b). As a result, more intensive deposition occurs on the south flank than on the north flank of the channel, which may underlie the higher siltation rate on the south flank (Fig. 10c).

In sum, the mobile CBS pool favours the sediment trapping in the middle reaches of the North Passage and on the south flank of the channel. This pattern of sediment transport helps to understand how sediment accumulates in an ebb-dominant estuary, favouring the maintenance of ETM and mouth bars in estuaries.

## 6. Conclusions

In this study, based on field observations in the North Passage of the Changjiang Estuary, we investigated the behaviour of CBS and provided information about the possible underlying mechanisms for the regime shift to hyper-turbid conditions. Historical observations (1988–2015) show a transition in SSC profiles after deepening, with decreasing SSC in mid-lower water columns and increasing SSC in the bottom layer. A positive feedback loop between vertical mixing and settling, combined with the feedback mechanisms hypothesised by Winterwerp and Wang (2013), might explain such a transition (Fig. 13). Our results provide indications for the presence of such a mechanism. The sediment accumulation in the estuary, generally driven by the processes proposed by Winterwerp and Wang (2013), enhances density stratification, upon which fine sediments are trapped near the bed due to turbulence damping and hindered settling. Then a snowball effect is initiated, favouring the formation of CBS and fluid mud. It suggests that the regime shift from low-turbid to hyper-turbid state is a result of the thickening of the CBS and/or fluid mud layer. Such a transition in SSC profiles is expected to be observed in other estuaries undergoing the regime shift.

After the deepening, a mobile CBS pool develops in the North Passage. Its location, length and thickness vary with tidal currents. It is located in the lower reaches at low-water slack and in the middle reaches at high-water slack, with an excursion of  $\sim 10$  km during the flood tide. Over a tidal cycle during spring tide, the pool has an averaged length of  $\sim 20$  km and a mean thickness of  $\sim 4$  m. The CBS mainly distributes in the Deepwater Navigational Channel; the CBS pool thus has a narrow width ( $< 1$  km). It is argued that the CBS on flanks of the channel results from the cross-channel movements of the CBS pool. The movements of the CBS pool, together with tidal asymmetry (e.g., slack-water asymmetry and lateral flow asymmetry), leads to sediment trapping in the middle reaches and on the south flank of the channel.

The observations by the bottom tripod show the response of the friction ( $f$ ) and drag coefficient ( $C_{D(z)}$ ) to sediment concentration. The

results show that both  $f$  and  $C_{D(z)}$  are constant and minimum in the presence of CBS. The drag reduction is up to 60–80%, which is higher than that observed in laboratory experiments. These observations also allow the verification of theoretical expressions for drag/friction coefficient by Wang (2002) and Winterwerp et al. (2009). The expression by Wang overestimates  $C_{D(z)}$  at high SSC; whereas the expression by Winterwerp et al. overestimates  $f$  at low SSC and underestimates  $f$  at high SSC. An empirical relationship was derived by fitting that can be used to predict friction coefficient and the magnitude of drag reduction for sediment transport studies.

## Declaration of Competing Interest

None.

## Acknowledgements

This work is supported by the National Natural Science Foundation of China (51739005) and the project 'Coping with deltas in transition' within the Programme of Strategic Scientific Alliance between China and The Netherlands (PSA), financed by the Ministry of Science and Technology of People's Republic of China (2016YFE0133700) and Royal Netherlands Academy of Arts and Sciences (KNAW) (PSA-SA-E-02). This study is also partly funded by the National Natural Science Foundation of China (41876091) and Shanghai Committee of Science and Technology (18DZ1206400; 19QA1402900). J. Lin thanks the China Scholarship Council (201706140180) for funding his visit at Delft University of Technology. Thanks to J. Gu, J. Zhao, L. Zhu, D. Zhang, C. Guo, Y. Chen, C. Xing, Z. Deng, J. Jiang, Y. Shen, Y. Zhang and J. Sun for their help in the field observations and inspirations in this research. We thank Prof. Edward Anthony and two anonymous reviewers for their constructive comments and suggestions.

## Appendix A. Appendix

When calculating the deposition of sediment from CBS, there is a wide range for the choice of gelling concentration ( $C_{gel}$ ). We considered five values (with  $C_{gel} = 60, 70, 80, 90$  and  $100 \text{ kg/m}^3$ ) and studied how this choice affected the final estimation of sediment settling from CBS. This sensitivity analysis shows that the net deposition of sediment from CBS is significantly affected by the gelling concentration (Fig. A1). When  $C_{gel}$  increases by  $10 \text{ kg/m}^3$ , the amount of sediment settling decreases by  $\sim 20\%$ . However, different choices of  $C_{gel}$  do not change the asymmetry of sediment deposition, i.e., much more sediment tends to deposit in the middle reaches than in the lower reaches of the channel.

## References

- Becker, M., Maushake, C., Winter, C., 2018. Observations of mud-induced periodic stratification in a hyperturbid estuary. *Geophys. Res. Lett.* 45, 5461–5469. <https://doi.org/10.1029/2018GL077966>.
- Bruens, A.W., Winterwerp, J.C., Kranenburg, C., 2012. Physical and numerical modeling of the entrainment by a high-concentration mud suspension. *J. Hydraul. Eng.* 138 (6), 479–490. [https://doi.org/10.1061/\(ASCE\)HY.1943-7900.0000545](https://doi.org/10.1061/(ASCE)HY.1943-7900.0000545).
- Burchard, H., Hetland, R.D., Schulz, E., Schuttelaars, H.M., 2011. Drivers of residual estuarine circulation in tidally energetic estuaries: straight and irrotational channels with parabolic cross section. *J. Phys. Oceanogr.* 41, 548–570. <https://doi.org/10.1175/2010JPO4453.1>.
- Burchard, H., Schuttelaars, H.M., Ralston, D.K., 2018. Sediment trapping in estuaries. *Annu. Rev. Mar. Sci.* 10, 371–395. <https://doi.org/10.1146/annurev-marine-010816-060535>.
- Changjiang Water Resources Commission (CWRC), 2014. *Bulletin of Yangtze River Sediment* <http://www.cjh.com.cn>. (in Chinese).
- Chanson, H., Trevelyan, M., Aoki, S., 2008. Acoustic Doppler velocimetry (ADV) in small estuary: field experience and signal post-processing. *Flow Meas. Instrum.* 19, 307–313. <https://doi.org/10.1016/j.flowmeasinst.2008.03.003>.
- Chen, W., de Swart, H.E., 2018. Longitudinal variation in lateral trapping of fine sediment in tidal estuaries: observations and a 3D exploratory model. *Ocean Dyn.* 68, 309–326. <https://doi.org/10.1007/s10236-018-1134-z>.
- Cheng, N.-S., 2015. Representative grain size and equivalent roughness height of a sediment bed. *J. Hydraul. Eng.* 123 (2), 149–152. [https://doi.org/10.1061/\(ASCE\)HY.1943-7900.0001069](https://doi.org/10.1061/(ASCE)HY.1943-7900.0001069).
- Chernetsky, A.S., Schuttelaars, H.M., Talke, S.A., 2010. The effect of tidal asymmetry and temporal settling lag on sediment trapping in tidal estuaries. *Ocean Dyn.* 60, 1219–1241. <https://doi.org/10.1007/s10236-010-0329-8>.
- Chow, V.T., 1959. *Open Channel Hydraulics*. McGraw-Hill Book Company, New York.
- Cloern, J.E., Foster, S.Q., Kleckner, A.E., 2014. Phytoplankton primary production in the world's estuarine-coastal ecosystems. *Bioecosystems* 11, 2477–2501. <https://doi.org/10.5194/bg-11-2477-2014>.
- Dankers, P.J.T., Winterwerp, J.C., 2007. Hindered settling of mud flocs: theory and validation. *Cont. Shelf Res.* 27, 1893–1907. <https://doi.org/10.1016/j.csr.2007.03.005>.
- de Jonge, V.N., Schuttelaars, H.M., van Beusekom, J.E.E., Talke, S.A., de Swart, H.E., 2014. The influence of channel deepening on estuarine turbidity levels and dynamics, as exemplified by the Ems estuary. *Estuar. Coast. Shelf Sci.* 139, 46–59. <https://doi.org/10.1016/j.ecss.2013.12.030>.
- Dijkstra, Y.M., Schuttelaars, H.M., Winterwerp, J.C., 2018. The hyperturbid state of the water column in estuaries and rivers: the importance of hindered settling. *Ocean Dyn.* 68, 377–389. <https://doi.org/10.1007/s10236-018-1132-1>.
- Dijkstra, Y.M., Schuttelaars, H.M., Schramkowski, G.P., Brouwer, R.L., 2019. Modeling the transition to high sediment concentrations as a response to channel deepening in the Ems River Estuary. *J. Geophys. Res. Ocean.* 124, 1–17. <https://doi.org/10.1029/2018JC014367>.
- Friedrichs, C.T., Wright, L.D., 1997. Sensitivity of bottom stress and bottom roughness estimates to density stratification, Eckernförde Bay, southern Baltic Sea. *J. Geophys. Res. Ocean.* 102 (C3), 5721–5732. <https://doi.org/10.1029/96JC03550>.
- Ge, J., Shen, F., Guo, W., Chen, C., Ding, P., 2015. Estimation of critical shear stress for erosion in the Changjiang Estuary: a synergy research of observation, GOCI sensing and modeling. *J. Geophys. Res. Ocean.* 120, 8439–8465. <https://doi.org/10.1002/2015JC010992>.
- Ge, J., Zhou, Z., Yang, W., Ding, P., Chen, C., Wang, Z.B., Gu, J., 2018. Formation of concentrated benthic suspension in a time-dependent salt wedge estuary. *J. Geophys. Res. Ocean.* 123, 8581–8607. <https://doi.org/10.1029/2018JC013876>.
- Geyer, W.R., 1993. The importance of suppression of turbulence by stratification on the estuarine turbidity maximum. *Estuaries* 16, 113–125. <https://doi.org/10.1007/BF02690231>.
- Guo, L., van der Wegen, M., Jay, D.A., Matte, P., Wang, Z.B., Roelvink, D., He, Q., 2015. River-tide dynamics: exploration of nonstationary and nonlinear tidal behavior in the Yangtze River estuary. *J. Geophys. Res. Ocean.* 120, 3499–3521. <https://doi.org/10.1002/2014JC010491>.
- Guo, C., He, Q., Guo, L., Winterwerp, J.C., 2017. A study of in-situ sediment flocculation in the turbidity maxima of the Yangtze Estuary. *Estuar. Coast. Shelf Sci.* 191, 1–9. <https://doi.org/10.1016/j.ecss.2017.04.001>.
- Guo, L., Su, N., Townend, I., Wang, Z.B., Zhu, C., Wang, X., Zhang, Y., He, Q., 2019. From the headwater to the delta: a synthesis of the basin-scale sediment load regime in the Changjiang River. *Earth-Sci. Rev.* 197, 102900. <https://doi.org/10.1016/j.earscirev.2019.102900>.
- Jiang, C., de Swart, H.E., Li, J., Liu, G., 2013. Mechanisms of along-channel sediment transport in the North Passage of the Yangtze Estuary and their response to large-scale interventions. *Ocean Dyn.* 63, 283–305. <https://doi.org/10.1007/s10236-013-0594-4>.
- Karimpour, F., Venayagamoorthy, S.K., 2014. A simple turbulence model for stably stratified wall-bounded flows. *J. Geophys. Res. Ocean.* 119, 870–880. <https://doi.org/10.1002/2013JC009622>.
- Kim, S.C., Friedrichs, C.T., Maa, J.P.Y., Wright, L.D., 2000. Estimating bottom stress in tidal boundary layer from Acoustic Doppler Velocimeter data. *J. Hydraul. Eng.* 126, 399–406. [https://doi.org/10.1061/\(ASCE\)0733-9429\(2000\)126:6\(399\)](https://doi.org/10.1061/(ASCE)0733-9429(2000)126:6(399)).
- Li, M.Z., Gust, G., 2000. Boundary layer dynamics and drag reduction in flows of high cohesive sediment suspensions. *Sedimentology* 47, 71–86. <https://doi.org/10.1046/j.1365-3091.2000.00277.x>.
- Li, Z., Jia, J., Wu, Y., Zong, H., Zhang, G., Wang, Y.P., Yang, Y., 2019. Vertical distributions of suspended sediment concentrations in the turbidity maximum zone of the periodically and partially stratified Changjiang Estuary. *Estuar. Coasts* 42, 1475–1490. <https://doi.org/10.1007/s12237-019-00616-z>.
- Lin, J., He, Q., Guo, L., van Prooijen, B.C., Wang, Z.B., 2020. An integrated optic and acoustic (IOA) approach for measuring suspended sediment concentration in highly turbid environments. *Mar. Geol.* 421, 106062. <https://doi.org/10.1016/j.margeo.2019.106062>.
- Liu, G., Zhu, J., Wang, Y., Wu, H., Wu, J., 2011. Tripod measured residual currents and sediment flux: impacts on the silting of the Deepwater Navigation Channel in the Changjiang Estuary. *Estuar. Coast. Shelf Sci.* 93, 192–201. <https://doi.org/10.1016/j.jecss.2010.08.008>.
- Liu, J., Cheng, H., Han, L., Wang, Z., 2019. Interannual variations on siltation of the 12.5-m deepwater navigation channel in Yangtze Estuary. *Adv. Water Sci.* 30 (1), 65–75. <https://doi.org/10.14042/j.cnki.32.1309.2019.01.007> (in Chinese with English abstract).
- Lu, Y., Lueck, R.G., 1999. Using a broadband ADCP in a tidal channel. Part I: mean flow and shear. *J. Atmos. Ocean. Technol.* 16, 1556–1567. [https://doi.org/10.1175/1520-0426\(1999\)016<1556:UABAIA>2.0.CO;2](https://doi.org/10.1175/1520-0426(1999)016<1556:UABAIA>2.0.CO;2).
- Manning, A.J., Langston, W.J., Jonas, P.J.C., 2010. A review of sediment dynamics in the Severn Estuary: influence of flocculation. *Mar. Pollut. Bull.* 61, 37–51. <https://doi.org/10.1016/j.marpolbul.2009.12.012>.
- Mehta, A.J., 1988. Laboratory studies on cohesive sediment deposition and erosion. In: Dronkers, J., van Leussen, W. (Eds.), *Physical Processes in Estuaries*. Springer, Berlin, Heidelberg, pp. 427–445. [https://doi.org/10.1007/978-3-642-73691-9\\_21](https://doi.org/10.1007/978-3-642-73691-9_21).
- Mellor, G.L., Yamada, T., 1974. A hierarchy of turbulence closure models for planetary boundary layers. *J. Atmos. Sci.* 31 (7), 1791–1806. [https://doi.org/10.1175/1520-0469\(1974\)031<1791:AHOTCM>2.0.CO;2](https://doi.org/10.1175/1520-0469(1974)031<1791:AHOTCM>2.0.CO;2).
- Munk, W.H., Anderson, E.R., 1948. Note on a theory of the thermocline. *J. Mar. Res.* 7, 276–295.
- Pu, X., Shi, J.Z., Hu, G.D., Xiong, L.B., 2015. Circulation and mixing along the North Passage in the Changjiang River Estuary, China. *J. Mar. Syst.* 148, 213–235. <https://doi.org/10.1016/j.jmarsys.2015.03.009>.
- Song, D., Wang, X.H., 2013. Suspended sediment transport in the Deepwater Navigation Channel, Yangtze River Estuary, China, in the dry season 2009: 2. Numerical simulations. *J. Geophys. Res. Ocean.* 118, 5568–5590. <https://doi.org/10.1002/jgrc.20411>.
- Soulsby, R.L., Dyer, K.R., 1981. The form of the near-bed velocity profile in a tidally accelerating flow. *J. Geophys. Res.* 86, 8067–8074. <https://doi.org/10.1029/JC086iC09p08067>.
- Stapleton, K.R., Huntley, D.A., 1995. Seabed stress determinations using the inertial dissipation method and the turbulent kinetic energy method. *Earth Surf. Process. Landf.* 20, 807–815. <https://doi.org/10.1002/esp.3290200906>.
- Talke, S.A., de Swart, H.E., de Jonge, V.N., 2009. An idealized model and systematic process study of oxygen depletion in highly turbid estuaries. *Estuar. Coasts* 32, 602–620. <https://doi.org/10.1007/s12237-009-9171-y>.
- Thompson, C.E.L., Amos, C.L., Angelaki, M., Jones, T.E.R., Binks, C.E., 2006. An evaluation of bed shear stress under turbid flows. *J. Geophys. Res. Ocean.* 111, C04008. <https://doi.org/10.1029/2005JC003287>.
- Uncles, R.J., Joint, I., Stephens, J.A., 1998. Transport and retention of suspended particulate matter and bacteria in the Humber-Ouse Estuary, United Kingdom, and their relationship to hypoxia and anoxia. *Estuarine Coast. Shelf Sci.* 21, 597–612. <https://doi.org/10.2307/1353298>.
- van Maren, D.S., Winterwerp, J.C., Vroom, J., 2015. Fine sediment transport into the hyper-turbid lower Ems River: the role of channel deepening and sediment-induced drag reduction. *Ocean Dyn.* 65, 589–605. <https://doi.org/10.1007/s10236-015-0821-2>.
- Wan, Y., Wang, L., 2017. Numerical investigation of the factors influencing the vertical profiles of current, salinity, and SSC within a turbidity maximum zone. *Int. J. Sediment Res.* 32, 20–33. <https://doi.org/10.1016/j.ijsrc.2016.07.003>.
- Wan, Y., Zhao, D., 2017. Observation of saltwater intrusion and ETM dynamics in a stably stratified estuary: the Yangtze Estuary, China. *Environ. Monit. Assess.* 189, 89. <https://doi.org/10.1007/s10661-017-5797-6>.
- Wan, Y., Wu, H., Roelvink, D., Gu, F., 2015. Experimental study on fall velocity of fine sediment in the Yangtze Estuary, China. *Ocean Eng.* 103, 180–187. <https://doi.org/10.1016/j.oceaneng.2015.04.076>.
- Wang, X.H., 2002. Tide-induced sediment resuspension and the bottom boundary layer in an idealized estuary with a muddy bed. *J. Phys. Oceanogr.* 32, 3113–3131. [https://doi.org/10.1175/1520-0485\(2002\)032<3113:TISRAT>2.0.CO;2](https://doi.org/10.1175/1520-0485(2002)032<3113:TISRAT>2.0.CO;2).
- Wang, L., 2010. *Tide Driven Dynamics of Subaqueous Fluid Mud Layers in Turbidity Maximum Zones of German Estuaries*. PhD thesis. University of Bremen.
- Wang, Z.Y., Larsen, P., Nestmann, F., Dittrich, A., 1998. Resistance and drag reduction of flows of clay suspensions. *J. Hydraul. Eng.* 124, 41–49. [https://doi.org/10.1061/\(ASCE\)0733-9429\(1998\)124:1\(41\)](https://doi.org/10.1061/(ASCE)0733-9429(1998)124:1(41)).
- Wang, Y., Yu, Q., Gao, S., 2011. Relationship between bed shear stress and suspended sediment concentration: Annular flume experiments. *Int. J. Sediment Res.* 26, 513–523. [https://doi.org/10.1016/S1001-6279\(12\)60009-2](https://doi.org/10.1016/S1001-6279(12)60009-2).
- Winterwerp, J.C., 2001. Stratification effects by cohesive and noncohesive sediment. *J. Geophys. Res.* 106, 22559–22574. <https://doi.org/10.1029/2000JC000435>.
- Winterwerp, J.C., 2002. Scaling parameters for high-concentrated mud suspensions in tidal flow. *Proc. Mar. Sci.* 5, 171–186. [https://doi.org/10.1016/S1568-2692\(02\)80015-8](https://doi.org/10.1016/S1568-2692(02)80015-8).
- Winterwerp, J.C., Wang, Z.B., 2013. Man-induced regime shifts in small estuaries - I: theory. *Ocean Dyn.* 63, 1279–1292. <https://doi.org/10.1007/s10236-013-0662-9>.
- Winterwerp, J.C., Lely, M., He, Q., 2009. Sediment-induced buoyancy destruction and drag reduction in estuaries. *Ocean Dyn.* 59, 781–791. <https://doi.org/10.1007/s10236-009-0237-y>.

- Winterwerp, J.C., Wang, Z.B., van Braeckel, A., van Holland, G., Kösters, F., 2013. Man-induced regime shifts in small estuaries - II: a comparison of rivers. *Ocean Dyn.* 63, 1293–1306. <https://doi.org/10.1007/s10236-013-0663-8>.
- Wu, J., Liu, H., Ren, J., Deng, J., 2011. Cyclonic spirals in tidally accelerating bottom boundary layers in the Zhujiang (Pearl River) Estuary. *J. Phys. Oceanogr.* 41, 1209–1226. <https://doi.org/10.1175/2011JPO4565.1>.
- Xing, C., 2016. A Study on Hydrodynamics and Sediment Transport Dynamics Between Flats and Channels in Estuary-A Case Study of North Passage Mouth Region in the Yangtze Estuary. MSc Thesis. East China Normal University, China (in Chinese with English abstract).
- Xu, J., 2009. Study on Near Bottom Dynamics and Sediment Processes in Turbidity Maximum. Master thesis. East China Normal University, China (in Chinese with English abstract).
- Yoshiyama, K., Sharp, J.H., 2006. Phytoplankton response to nutrient enrichment in an urbanized estuary: apparent inhibition of primary production by overeutrophication. *Limnol. Oceanogr.* 51, 424–434. [https://doi.org/10.4319/lo.2006.51.1\\_part\\_2.0424](https://doi.org/10.4319/lo.2006.51.1_part_2.0424).
- Zhou, Z., Ge, J., Wang, Z.B., van Maren, D.S., Ma, J., Ding, P., 2019. Study of lateral flow in a stratified tidal channel-shoal system: the importance of intratidal salinity variation. *J. Geophys. Res. Ocean.* 124, 6702–6719. <https://doi.org/10.1029/2019jc015307>.
- Zhu, J., Ding, P., Zhang, L., Wu, H., Cao, H., 2006. Influence of the deep waterway project on the Changjiang Estuary. In: Wolanski, E. (Ed.), *The Environment in Asia Pacific Harbours*. Springer, Dordrecht, pp. 79–92. [https://doi.org/10.1007/1-4020-3655-8\\_6](https://doi.org/10.1007/1-4020-3655-8_6).
- Zhu, Q., van Prooijen, B.C., Wang, Z.B., Ma, Y.X., Yang, S.L., 2016. Bed shear stress estimation on an open intertidal flat using in situ measurements. *Estuar. Coast. Shelf Sci.* 182, 190–201. <https://doi.org/10.1016/j.ecss.2016.08.028>.
- Zhu, L., He, Q., Shen, J., 2018. Modeling lateral circulation and its influence on the along-channel flow in a branched estuary. *Ocean Dyn.* 68, 177–191. <https://doi.org/10.1007/s10236-017-1114-8>.
- Zhu, C., Guo, L., van Maren, D.S., Tian, B., Wang, X., He, Q., Wang, Z.B., 2019. Decadal morphological evolution of the mouth zone of the Yangtze Estuary in response to human interventions. *Earth Surf. Process. Landf.* 44, 2319–2332. <https://doi.org/10.1002/esp.4647>.